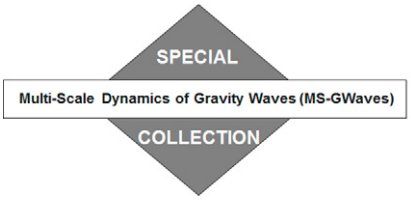

Global Distributions of Tropospheric and Stratospheric Gravity Wave Momentum Fluxes Resolved by the 9-km ECMWF Experiments

JUNHONG WEI,[a,b,c] FUQING ZHANG,[d,e] JADWIGA H. RICHTER,[f] M. JOAN ALEXANDER,[g] AND Y. QIANG SUN[h,i]

[a] *School of Atmospheric Sciences, Sun Yat-sen University, Zhuhai, China*
[b] *Guangdong Province Key Laboratory for Climate Change and Natural Disaster Studies, Sun Yat-sen University, Zhuhai, China*
[c] *Southern Marine Science and Engineering Guangdong Laboratory (Zhuhai), Zhuhai, China*
[d] *Department of Meteorology and Atmospheric Science, The Pennsylvania State University, University Park, Pennsylvania*
[e] *Center for Advanced Data Assimilation and Predictability Techniques, The Pennsylvania State University, University Park, Pennsylvania*
[f] *National Center for Atmospheric Research, Boulder, Colorado*
[g] *CoRA Office, NorthWest Research Associates, Inc., Boulder, Colorado*
[h] *NOAA/Geophysical Fluid Dynamics Laboratory, Princeton, New Jersey*
[i] *Cooperative Institute for Modeling the Earth System, Program in Oceanic and Atmospheric Sciences, Princeton University, Princeton, New Jersey*

(Manuscript received 26 June 2021, in final form 26 April 2022)

ABSTRACT: Based on 20-day control forecasts by the 9-km Integrated Forecasting System (IFS) at the European Centre for Medium-Range Weather Forecasts (ECMWF) for selected periods of summer and winter events, this study investigates global distributions of gravity wave momentum fluxes resolved by the highest-resolution-ever global operational numerical weather prediction model. Two supplementary datasets, including 18-km ECMWF IFS experiments and the 30-km ERA5, are included for comparison. In the stratosphere, there is a clear dominance of westward momentum fluxes over the winter extratropics with strong baroclinic instability, while eastward momentum fluxes are found in the summer tropics. However, meridional momentum fluxes, locally as important as the above zonal counterpart, show different behaviors of global distribution characteristics, with northward and southward momentum fluxes alternating with each other especially at lower altitudes. Both events illustrate conclusive evidence that stronger stratospheric fluxes are found in the ECMWF forecast with finer resolution, and that ERA5 datasets have the weakest signals in general, regardless of whether regridding is applied. In the troposphere, probability distributions of vertical motion perturbations are highly asymmetric with more strong positive signals especially over latitudes covering heavy rainfall, likely caused by convective forcing. With the aid of precipitation accumulation, a simple filtering method is proposed in an attempt to eliminate those tropospheric asymmetries by convective forcing, before calculating tropospheric wave-induced fluxes. Furthermore, this research demonstrates promising findings that the proposed filtering method could help in reducing the potential uncertainties with respect to estimating tropospheric wave-induced fluxes. Finally, absolute momentum flux distributions with proposed approaches are presented, for further assessment in the future.

KEYWORDS: Convection; Dynamics; Gravity waves; Mesoscale processes; Momentum; General circulation models

1. Introduction

The signals and the life cycles of atmospheric gravity waves have been documented in many studies, using observations (Wang and Geller 2003; Plougonven et al. 2003; Gong et al. 2012; Zhang et al. 2015), numerical investigations of observed cases (Zhang et al. 2013; Qian et al. 2020), and idealized simulations (Zhang 2004; Wang et al. 2009; Wei and Zhang 2014, 2015; Wei et al. 2016). It is well established that gravity waves play a key role in atmospheric dynamics on various spatial and temporal scales. For instance, gravity waves can trigger and modulate tropospheric weather (Zhang et al. 2001; Lane and Zhang 2011; Du et al. 2021; Ruppert et al. 2022) and clear-air turbulence (Shapiro 1980; Lane et al. 2004; Koch et al. 2005). Furthermore, gravity waves can contribute significantly to building the atmospheric energy spectra (Callies et al. 2014; Bierdel et al. 2016; Sun et al. 2017), and they are also found to likely link small-scale small-amplitude initial errors to rapid upscale error growth and thus limit mesoscale predictability (Zhang et al. 2007; Sun and Zhang 2016; Bierdel et al. 2018).

Supplemental information related to this paper is available at the Journals Online website: https://doi.org/10.1175/JAS-D-21-0173.s1.

Zhang: Deceased

Sun's current affiliation: Department of Mechanical Engineering, Rice University, Houston, Texas.

Corresponding author: Junhong Wei, weijunh@mail.sysu.edu.cn

DOI: 10.1175/JAS-D-21-0173.1

Gravity waves also play an important role in the large-scale circulation of the middle and upper atmosphere, as they can travel long distances from their sources and transfer significant amounts of momentum and energy to higher altitudes (Holton and Lindzen 1972; Houghton 1978; Lindzen 1981; Dunkerton and Butchart 1984; Andrews et al. 1987; Holton et al. 1995; Richter et al. 2010; Limpasuvan et al. 2012; Butchart 2014). Nowadays, gravity wave parameterizations (e.g., Lott and Miller 1997; Alexander and Dunkerton 1999; Warner and McIntyre 2001) are needed in most global numerical weather prediction (NWP) models to represent their impacts on the large-scale flows (Fritts and Alexander 2003; Kim et al. 2003), since the resolution required to resolve the full gravity wave spectrum is orders of magnitude higher than what is applied in many current atmospheric general circulation models (GCMs). However, due to gaps in its physical understanding together with the need for computational efficiency, existing parameterization schemes still use many oversimplifications and tunable parameters (Haynes 2005; Richter et al. 2010; Wei et al. 2019; Plougonven et al. 2020), including the gravity wave source specification (Alexander et al. 2010), the assumption of instantaneous gravity wave propagation (Bölöni et al. 2016) and one-dimensional vertical propagation (Ribstein et al. 2015), the neglect of secondary wave generation (Becker and Vadas 2018; Wilhelm et al. 2018), and gravity wave intermittency (de la Cámara et al. 2014; Minamihara et al. 2020).

With developments in computational technology and NWP (Bauer et al. 2015, 2021), one important source to better understand gravity wave dynamics and its global impact is the high-resolution GCM, because an important range of the gravity wave spectrum can be considered as resolved. It has been demonstrated by many studies that realistic features of gravity waves and/or large-scale circulations could be reproduced in some high-resolution GCMs, such as the WACCM-SE model with a horizontal resolution of ~0.25° and a model top at ~145-km altitude (Liu et al. 2014), the Kanto model with a 0.56° horizontal resolution and a model top at 85-km altitude (Watanabe et al. 2008), and the CAM5 (Neale et al. 2010) with a grid of 0.238° × 0.318° and a model top at ~40-km altitude (Geller et al. 2013). In particular, by comparing absolute zonal-mean gravity wave pseudo-momentum fluxes among different datasets, Geller et al. (2013) also point out that the observed behavior of decreasing fluxes toward the poles is well captured by the high-resolution models such as Kanto and CAM5, in contrast to the coarse-grid GCMs using non-orographic gravity wave parameterizations with deficient source specification. Furthermore, global convection-permitting models, such as the 7-km simulation of *GOES-5* Nature Run (Holt et al. 2017), continue to demonstrate realistic global patterns in gravity wave characteristics compared to the observations. Nonetheless, based on the first intercomparison of resolved gravity wave pseudo-momentum fluxes in various global convection-permitting simulations (Stephan et al. 2019a), magnitudes of the fluxes differ substantially among experiments.

Arguably, the most advanced numerical weather prediction model system is developed and operated at the European Centre for Medium-Range Weather Forecasts (ECMWF). Many studies showed that the ECMWF (re)analyses (e.g., Jewtoukoff et al. 2015; Gupta et al. 2021) and/or forecasts (e.g., Stephan et al. 2019a; Kaifler et al. 2020) could realistically capture the structure and amplitude of mesoscale gravity waves, in comparison with field campaign observations such as those from DEEPWAVE (Fritts et al. 2016), superpressure balloon observations (Jewtoukoff et al. 2015), satellite observations (Yamashita et al. 2010; Shutts and Vosper 2011; Hoffmann et al. 2017), lidar observations (Ehard et al. 2018; Kaifler et al. 2020), and so on. The latest update of ECMWF operational model to horizontal grid spacing of approximately 9 km allows even more detailed resolution of gravity wave mesoscale structures, and thus is an excellent resource for investigating the global distributions of the fluxes induced by the resolved gravity waves (also read the ECMWF Technical Memorandum by Polichtchouk et al. 2021). Using such unprecedented high-resolution global models, the predictability limit of midlatitude weather has recently been studied by Zhang et al. (2019). However, that work did not address the characteristics of the resolved gravity waves, especially in comparison with the previous operational version at ~18-km horizontal grid spacing and the latest reanalysis datasets from ECMWF. Furthermore, past studies on the global distributions of wave-induced fluxes by the high-resolution GCMs were primarily focused on the stratosphere and/or the mesosphere, whereas the corresponding distributions in the troposphere have often been neglected. The reason for this disproportionate and inadequate attention by the community, which hinders a complete understanding of the characteristics of wave-induced fluxes in the troposphere from which region parameterized wave sources are launched in many operational global models (e.g., Plougonven et al. 2020), may be partly due to 1) difficulties in obtaining the perturbations induced by gravity waves instead of other processes at the same or similar scale (e.g., moist processes highlighted in Alexander et al. (2006); small-scale synoptic waves highlighted in Wedi et al. 2020), and 2) the general lack of suitable global observation datasets as ground-truth for model validation.

The goals of the present study, complementary to Zhang et al. (2019), are 1) to investigate the global distributions of tropospheric and stratospheric gravity wave momentum fluxes resolved by three different products from ECMWF based on a selected flux calculation method, and 2) to identify the potential uncertainties associated with the above calculated fluxes especially in the troposphere and propose a simple filtering method to statistically and effectively reduce the above uncertainties from large datasets by high-resolution global forecasts and/or analyses. A better understanding of the global distributions of gravity wave momentum fluxes resolved in a state-of-the-art global NWP model will be of great value to the community of gravity wave research in improving the knowledge of gravity wave dynamics (Preusse et al. 2014; Stephan et al. 2019a; Wedi et al. 2020), as well as in providing guidance to parameterizations of gravity waves in coarser-resolution global weather and climate models (Plougonven et al. 2020). For example, characteristics of gravity waves resolved by the ECMWF model have been previously documented in Preusse

et al. (2014), based on its model version back in 2008. By investigating the temporal variability in the total hemispheric flux, remarkable day-to-day variations of a factor of 3 are identified in their work, being higher than what was reported from quasi-hemispheric mesoscale modeling (Plougonven et al. 2013).

This article is arranged as follows. A brief introduction to the data and method used for the work will be shown in section 2, followed in section 3 by the analysis of gravity wave momentum flux distribution in the stratosphere. Section 4 will present the corresponding tropospheric results. This section will also identify the potential calculation errors which could be caused by convective forcing. A simple tentative filtering method based on the information of precipitation accumulation will be proposed in an attempt to efficiently minimize those errors in high-resolution global datasets. Furthermore, the global distribution comparison based on two techniques with different formulas for the expression of the absolute momentum flux will be explored in section 5, which demonstrates promising and encouraging evidence that the above filtering method could improve flux estimation in the troposphere. Section 6 contains a summary.

2. Data and method

a. *Global numerical simulations and reanalysis datasets*

The data employed in this study directly come from the 20-day control forecast by the 9-km operational model IFS (IFS cycle 41R2; Wedi 2014; Malardel et al. 2016) at ECMWF described in Zhang et al. (2019). This new ECMWF IFS model implements a cubic octahedral reduced Gaussian grid with spectral truncation denoted by Tco1279, instead of the linear reduced Gaussian grid. The octahedral grid is globally more uniform than the linear reduced Gaussian grid. In the vertical, the ECMWF model has 137 levels and a model top at 0.01 hPa. This resolution upgrade results in the highest-resolution-ever global operational NWP model at the time of the publication of Zhang et al. (2019). The physical parameterizations (Orr et al. 2010) follow the operational setup, with adopting orographic (Lott and Miller 1997) and non-orographic (Scinocca 2003) gravity wave drag parameterizations, in addition to parameterizations of shallow, midlevel, and deep convection (Bechtold et al. 2008). To prevent artificial wave reflection from the model top, the wavenumber-dependent fourth-order diffusion is employed for a very weak stratospheric sponge from 10 hPa. These 9-km ECMWF experiments also include two additional sponge layers, including a very strong mesospheric sponge for the divergence from 1 hPa to the model top and a sponge at the top three levels for the vorticity.

Two supplementary datasets are adopted for comparison, including the corresponding 18-km forecasts by the previous version of the operational model IFS at ECMWF and the 30-km reanalysis datasets by ERA5. Note that the 18-km ECMWF IFS experiments (IFS cycle 41R2, Tco639) have a model formulation the same as that of the 9-km ECMWF IFS experiments, except for the resolution. Also, the 30-km ERA5 global dataset (Hersbach et al. 2020) can be found on the official website of ECMWF at https://www.ecmwf.int/en/forecasts/datasets/reanalysis-datasets/era5.

b. *Two event periods studied by Zhang et al. (2019) and the current research*

Two event periods in boreal winter and summer were chosen and studied by Zhang et al. (2019), and both of them will be analyzed in the current research. The selection of those two events is somewhat subjective but with the intent to represent the typical midlatitude predictability while covering two recent hazardous regional weather events, including a wintertime strong cold-surge event affecting northern Europe in early January 2016 and a summertime historic rainfall-flooding event in China during July 2016. For simplicity, they are hereafter referred to as winter case and summer case, respectively. Note that the winter case, covering an interesting period with extensive gravity wave literature based on measurements (Bramberger et al. 2018; Dörnbrack et al. 2018; Ehard et al. 2018; Bossert et al. 2020) and analyses/forecasts (Dörnbrack et al. 2018; Dörnbrack 2021), also corresponds to an extreme El Niño period (Blunden and Arndt 2016), as well as the coldest and strongest Arctic polar vortex for almost 70 years (Matthias et al. 2016). The 9-km ECMWF IFS experiments are initialized from the operational analysis by ECMWF and integrated forward for 20 days covering 0000 UTC 25 December 2015–0000 UTC 14 January 2016 and 0000 UTC 25 June–0000 UTC 15 July 2016, respectively. The instantaneous output at 0000 and 1200 UTC during the above periods are saved for all the computations in the current study, while the first 48 h are excluded to allow for enough spinup time (Stephan et al. 2019a).

To illustrate the meteorological situation for both cases by the 9-km ECMWF IFS experiments, global distributions of the mean 12-h precipitation accumulation are shown in Fig. 1. The precipitation is active and widespread throughout the tropics, especially over the ocean. Strong convective signals are recorded over the midlatitude ocean of the Northern Hemisphere in the winter case, while the simulations have successfully captured the heavy rainfall peaks over Asia in the summer case. Note that neither case has apparent severe weather outbreaks reported in the midlatitude atmosphere of the Southern Hemisphere (Zhang et al. 2019), although the midlatitude convective zone during the austral wintertime (Fig. 1b) is more widespread than that during the austral summertime (Fig. 1a).

c. *Six representative altitudes from troposphere and stratosphere in the current research*

A total of six representative altitudes are selected in the current study to examine the resolved gravity waves from the troposphere and the stratosphere, including the vertical levels at 500, 300, 200, 100, 50, and 10 hPa. To facilitate effective discussions in the present article, the lower three layers are classified into the category of the troposphere, while the upper three layers are grouped together under stratosphere. Here, the altitude at 100 hPa is still loosely categorized into the stratosphere even though it is close to the tropopause

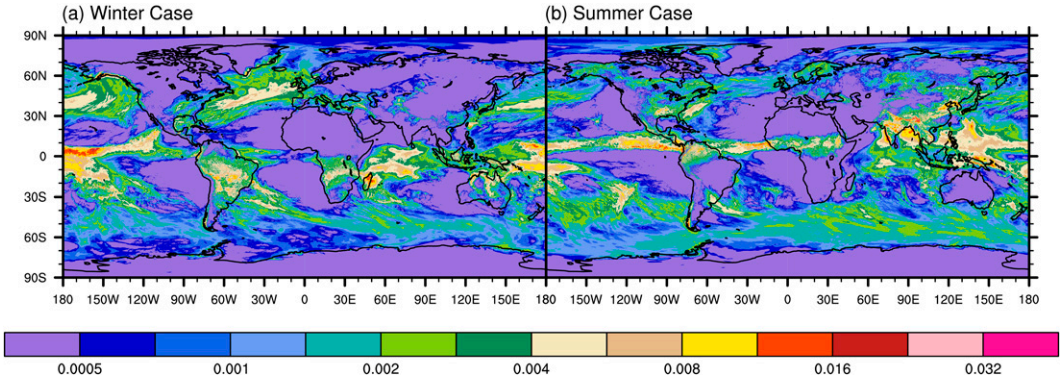

FIG. 1. The global distributions of the 20-day mean 12-h precipitation accumulation (unit: m) averaged for (a) the winter case and (b) the summer case. The calculations are based on the 20-day control forecast by the 9-km operational model Integrated Forecasting System (IFS; IFS cycle 41R2, Tco1279) at the European Centre for Medium-Range Weather Forecasts (ECMWF) described in Zhang et al. (2019). The abovementioned simulation for the winter case is initialized at 0000 UTC 25 Dec 2015, while that for the summer case is initialized at 0000 UTC 25 Jun 2016. The computations for the time averaging use the instantaneous output at 0000 and 1200 UTC of all available days.

over the tropics. In addition, caution should be taken for the wave analysis at 10 hPa, as it lies at the bottom of the weak stratospheric sponge prescribed in the model. Figure 2 shows the global distributions of the mean zonal wind at the above six representative altitudes from the troposphere and the stratosphere. Compared with the summer hemisphere, the background field of the middle latitudes in the winter hemisphere is characterized by the westerlies that are much stronger and more consistent from the troposphere to the stratosphere, with remarkable enhancements around 200 and 10 hPa (especially in the winter case). In contrast, the tropical background flow is distinguishable by a much weaker wind signal in the troposphere, with an easterly phase of the stratospheric quasi-biennial oscillation (e.g., Lu et al. 2020) especially identifiable at 10 hPa.

d. *The selected method of obtaining resolved gravity wave momentum fluxes from global datasets*

An exact calculation of the vertical flux of zonal and meridional momentum (i.e., $\rho_0\overline{u'w'}$ and $\rho_0\overline{v'w'}$, respectively) by the resolved gravity waves usually requires high-frequency model output (on the order of 10 min or less) for spectral analysis of the wind field in space and time, as explained in Stephan et al. (2019a). However, due to the limitation of data availability, this is not always feasible when processing such large datasets from high-resolution GCMs. Instead in many studies (e.g., Geller et al. 2013; Holt et al. 2017; Stephan et al. 2019a; Chun et al. 2019), the computations of the resolved wave-induced fluxes have been performed individually for each available instantaneous model output. To achieve this, two important procedures need to be clarified and discussed in the following paragraphs.

The first procedure is to extract the resolved gravity wave perturbations at each single time step. Here, it is often assumed that a given variable can be expanded into a steady or slowly varying large-scale background state and a perturbation presumably induced by gravity wave at a shorter scale in time and space (e.g., $u = \overline{u} + u'$ for the zonal velocity component). There are at least two major approaches to quantify the gravity wave perturbations (also refer to Mirzaei et al. 2017 on this topic) based on the two-dimensional and/or three-dimensional datasets in space (e.g., Lehmann et al. 2012), including a dynamical approach which often attempts to link the wave diagnostics with a certain balance relation and/or dynamical constraint (e.g., Hien et al. 2018) and a statistical approach which typically applies a spectral filtering or a spatial smoothing to retrieve the gravity wave signals based on the scale separation assumption between the background state and the perturbation (e.g., Wei et al. 2016).

The second procedure concerns the evaluation of the interaction terms between wave perturbations, which in this case refer to the interactions of zonal and meridional wind perturbations, respectively, with the vertical wind perturbation (i.e., $\overline{u'w'}$ and $\overline{v'w'}$). Here, the overlines above the products of the perturbations indicate a spatial average which is usually over one or a small number of wavelength(s), assuming the wave is locally monochromatic. Note that a pure pointwise computation for the above quadratic quantities without the procedure of the above overlines is not physically meaningful. In this regard, it is useful in practice to utilize low-pass filtering or areal smoothing (e.g., Kruse and Smith 2015), and some studies even define the overlines simply as the zonal mean (e.g., Sato et al. 2018), in order to investigate the wave impacts from a global perspective.

An extensive survey, with details shown in the appendix, has been conducted to investigate the sensitivities of the resolved flux calculations to different available choices, before finalizing the procedures for obtaining momentum fluxes in the current study, which are in the end performed in a hybrid manner of both dynamical approach and statistical approach. First, in order to better focus on the unbalanced gravity wave dynamics, the divergent components of the winds (e.g., u_{DIV}) are extracted by the Helmholtz decomposition technique, before any spatial

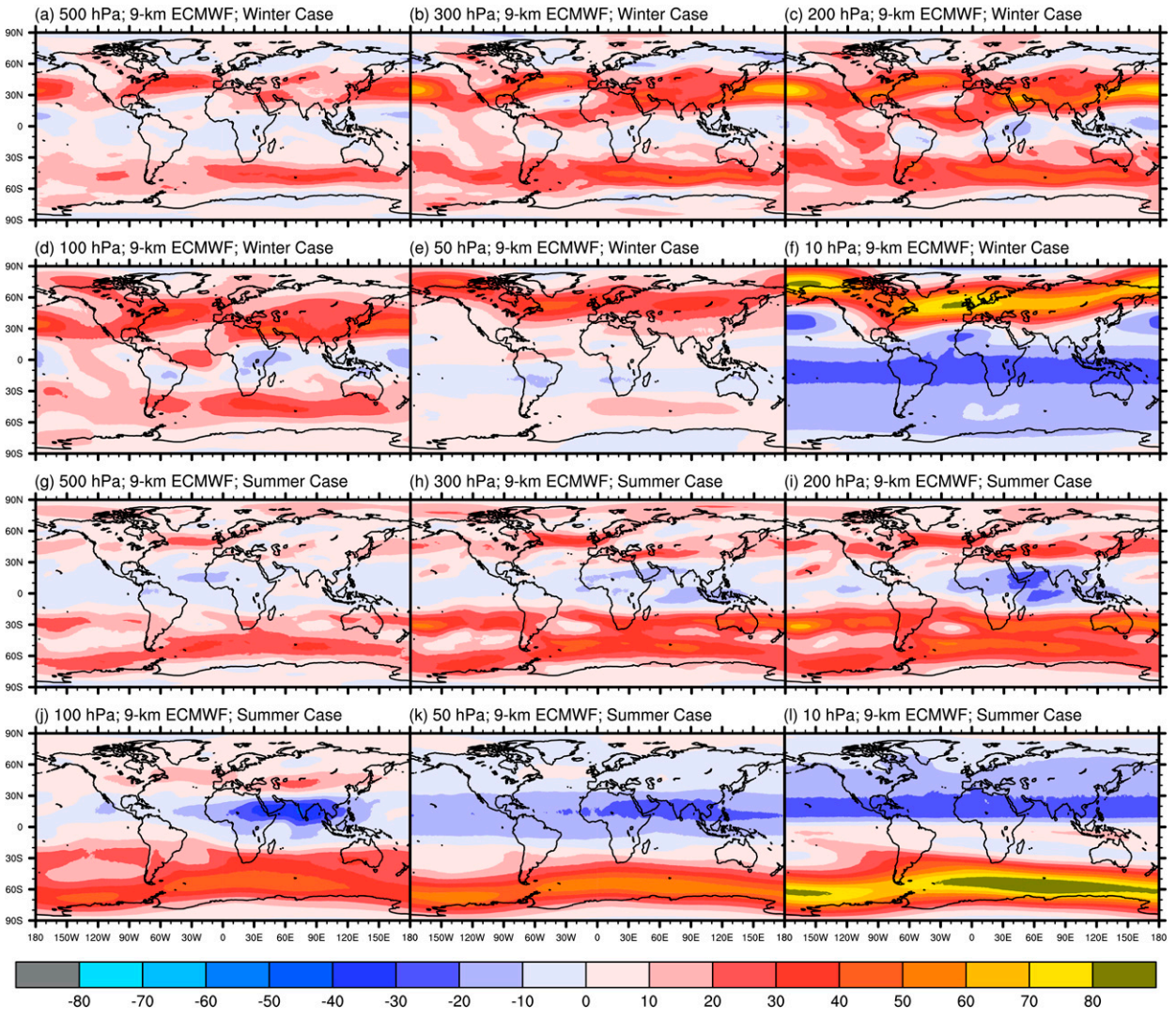

FIG. 2. The global distributions of the 20-day mean zonal wind (unit: m s^{-1}) averaged for (a)–(f) the winter case and (g)–(l) the summer case at the six selected altitudes from troposphere and stratosphere, including (a),(g) 500; (b),(h) 300; (c),(i) 200; (d),(j) 100; (e),(k) 50; and (f),(l) 10 hPa. The calculations are based on the 20-day control forecast by the operational 9-km ECMWF IFS model (IFS cycle 41R2, Tco1279) described in Zhang et al. (2019).

filtering/smoothing method is applied. Second, the overline computation in the first procedure (i.e., retrieving the background state) is defined as the spectrally truncated retrieval of total wavenumbers ≤ 40 in the spherical harmonic expansion (e.g., $u' = u_{\mathrm{DIV}} - (u_{\mathrm{DIV}})_{\mathrm{ST}_{l\leq 40}}$; also read Wedi et al. 2020). Third, the overline computation in the second procedure (i.e., the smoothing of the quadratic quantities) is defined as the $5^\circ \times 5^\circ$ latitude–longitude horizontal running average (e.g., $\overline{u'w'} = (u'w')_{\mathrm{Boxcar\_Smth}}$; also read Chun et al. 2019).

3. Stratospheric momentum flux distribution based on the selected flux calculation method

Based on three different global datasets, Fig. 3 demonstrates the global distributions of the net stratospheric time-mean zonal momentum flux per unit volume averaged for the winter case and the summer case, respectively. At the altitude of 100 hPa, the 9-km ECMWF IFS model (Figs. 3a,j) shows a clear dominance of negative momentum fluxes (i.e., westward momentum fluxes) over the middle latitudes, especially above the broad belt of midlatitude winter storm tracks associated with strong baroclinic instability and precipitation (e.g., Hendricks et al. 2014). Local enhancement of the westward momentum fluxes over the mountainous areas (e.g., the Andes; also read Kruse et al. 2022) can also be identified over the middle latitudes for both cases. In contrast, the intertropical convergence zone, where tropospheric zonal wind is weak (Fig. 2), is characterized by positive (i.e., eastward) momentum fluxes. The above general pattern with westward momentum fluxes in

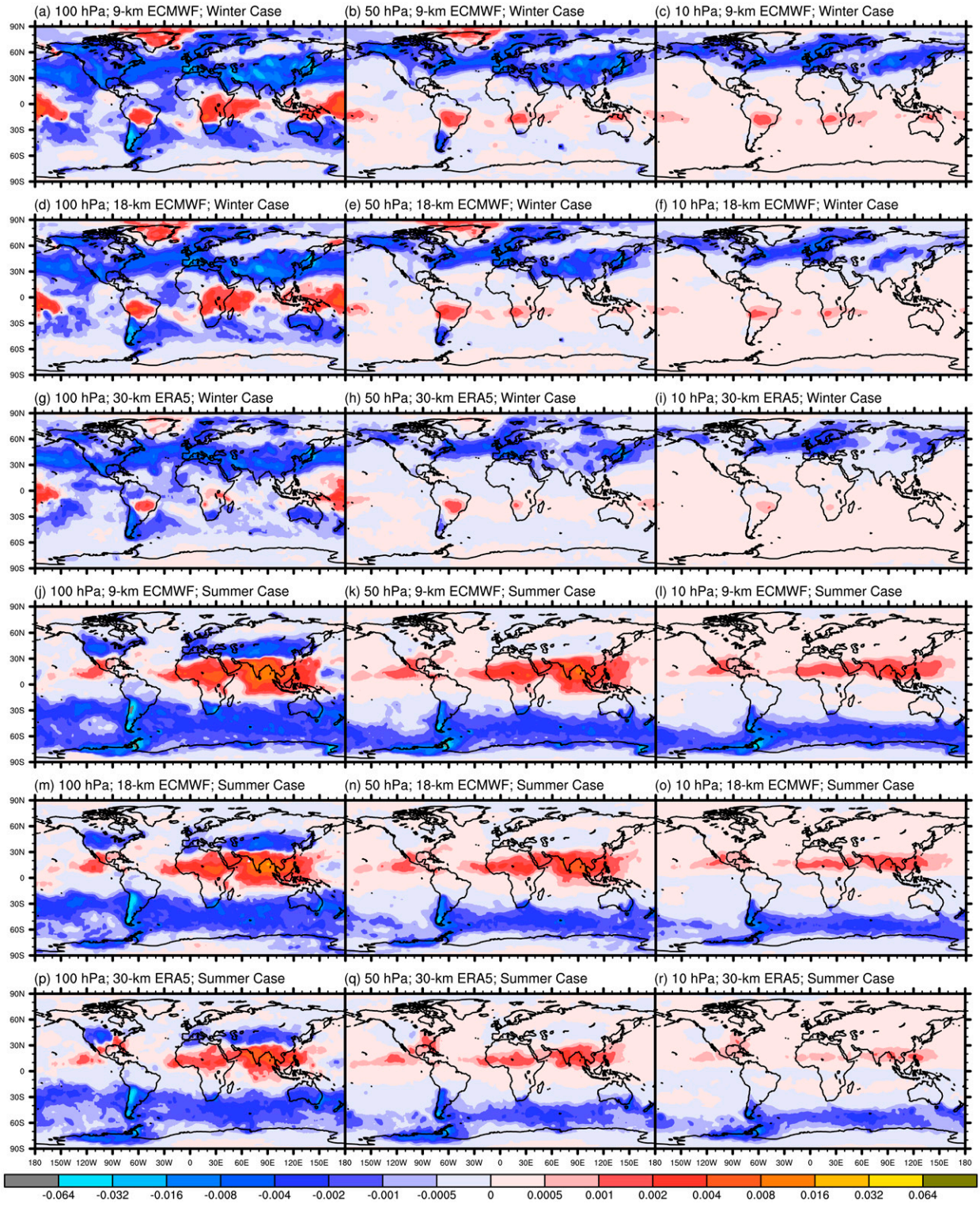

FIG. 3. The global distributions of the 20-day mean zonal momentum flux per unit volume $\rho_0\overline{u'w'}$ (unit: Pa) averaged for (a)–(i) the winter case and (j)–(r) the summer case at the three selected altitudes from stratosphere, including (left) 100, (center) 50, and (right) 10 hPa. Note that 100 hPa is loosely categorized into the group of the stratosphere in the current study. For comparison, three datasets with different resolutions are used in the calculations, including (a)–(c),(j)–(l) the 20-day control forecast by the operational 9-km ECMWF IFS model (IFS cycle 41R2, Tco1279) described in Zhang et al. (2019); (d)–(f),(m)–(o) that by the 18-km ECMWF IFS (IFS cycle 41R2, Tco639); and (g)–(i),(p)–(r) the reanalysis datasets by the 30-km ERA5 (Hersbach et al. 2020).

the winter extratropics and eastward momentum fluxes in the summer tropics, also revealed by other references (e.g., Sato et al. 2009; Chun et al. 2019), appears at all heights (Figs. 3b,k for 50 hPa; Figs. 3c,3l for 10 hPa). However, due to the wave filtering by background wind and/or the wave breaking associated with the decreasing density, those fluxes, especially the lower-latitude parts of the negative signals, dramatically decrease with height. In comparison, a similar pattern can also be found in the 18-km ECMWF IFS model (second row and fifth row) and the 30-km ERA5 datasets (third row and sixth row), although it is evident that the ECMWF datasets with coarser resolution correspond to weaker signals of the stratospheric zonal momentum fluxes. Note that potential source mechanisms of the gravity waves in the winter extratropics include mountains and non-orographic sources (e.g., moist jet–front systems), while convection is commonly considered as the primary source in the tropics.

The corresponding distribution of the net stratospheric mean meridional momentum fluxes (Fig. 4) is quite different from the zonal ones, especially at the lower altitude. For example, for the winter case at 100 hPa, positive and negative fluxes (i.e., northward and southward momentum fluxes) oscillate in longitude at almost all latitudes in all datasets. This is also true for the summer case, except that the middle latitudes of the winter hemisphere are distinguished by negative fluxes. Nonetheless, the above pattern at 100 hPa, featured by the fluxes with no clear dominant sign, turns into a more organized picture via filtering with height increasing up to 10 hPa, at which tropical fluxes almost vanish and only fluxes at middle and high latitudes are noticeable. Note that in the winter case there is still a change in sign over the high latitudes between North America and North Atlantic. Besides, the resolved gravity wave fluxes also suggest a tendency of meridional convergence into the winter jet, a feature of lateral wave propagation highlighted by several previous studies (e.g., Sato et al. 2009; Holt et al. 2017; Stephan et al. 2019a; Hindley et al. 2020).

Figure 5 further compares the zonal means of net stratospheric zonal and meridional momentum fluxes among three different datasets. Although similar in general behavior, the zonal-mean profiles again demonstrate that the strongest signals can be found in the 9-km ECMWF IFS model with the highest resolution. For the zonal momentum fluxes, the local peak in the 9-km ECMWF IFS model can be stronger than the 18-km ECMWF IFS model by a factor of approximately 5.8 (e.g., around 70S at 100 and 50 hPa in the summer case; also read Kruse et al. 2022). For the meridional momentum fluxes, the agreement between the 9-km ECMWF IFS model and the 18-km ECMWF IFS model is noticeably better than for the zonal fluxes. Although the sign of the meridional fluxes varies along the meridional direction, those fluxes are not negligible, since they can still be locally comparable to the zonal counterpart. It is also interesting to point out the broad pattern agreement with the recent satellite study from Hindley et al. (2020) (our Fig. 5 versus their Figs. 1a,b), although there is no apparent sign alternation with wintertime meridional fluxes at their interested altitude in Northern Hemisphere (e.g., around year = 2016 in their Fig. 1d). Understandably, the ERA5 datasets have the weakest signals over almost all latitudes in both seasons. This should be due to 1) its coarse resolution, and 2) the applied data assimilation method which tends to filter out gravity waves significantly (e.g., Greybush et al. 2011). Furthermore, by interpolating the global datasets into the same horizontal grid, tests have been performed in order to understand the effects of model resolution, which again supports the above findings (details in appendix section e).

4. Tropospheric momentum flux distribution

a. Results based on the selected flux calculation method

The corresponding results in the troposphere are also studied based on the same flux calculation method. As an example, the zonal-mean flux profiles in the troposphere are shown in Fig. 6, which can be directly compared with Fig. 5 (i.e., the stratospheric profiles). Whereas ECMWF forecasts in the stratosphere tend to diverge from each other, the most striking feature in the troposphere is their overall consistency, except for the zonal momentum fluxes around 70S in the summer case. Here, as also highlighted and discussed in appendix section d, it should be kept in mind that the assumption of the dominance by the upward-only gravity wave propagation may not be valid in the troposphere.

Based on the 9-km ECMWF IFS model, Fig. 7 further compares the global distributions of the mean absolute momentum flux per unit volume (M) between troposphere and stratosphere. Here, M is calculated based on the following equation:

$$M = \sqrt{\rho_0^2[(\overline{u'w'})^2 + (\overline{v'w'})^2]}, \tag{1}$$

where ρ_0 is the background density, (u', v', w') is the vector of wind perturbations. The global distribution of the absolute momentum flux averaged over the selected periods (Fig. 7) can well reproduce the predominant features from both zonal and meridional fluxes (Figs. 3 and 4), including many important hot spots of interest (e.g., the Andes).

b. Potential calculation errors in the troposphere

One important assumption for the above flux estimation is that small-scale perturbations are induced by gravity waves. However, calculation errors could be introduced if this premise is false. Take the 9-km ECMWF IFS model as an example, Fig. 8 demonstrates the probability distributions of the vertical motion perturbation in the troposphere, in order to validate the interpretation of obtained signals as free waves. Here, a notable asymmetry about zero is evident from the higher probability of strong positive vertical motions especially over latitudes covering heavy rainfall, such as summer tropics and Asia in the summer case (Fig. 1). The 18-km ECMWF IFS experiment replicates this salient characteristic in the troposphere (not shown), although such an asymmetric feature is less pronounced, illustrating a sensitivity to resolution associated with the simulated convection (Powers 1997; Wei and Zhang 2014). In another recent sensitivity investigation based on two 5-km global simulations with explicit and parameterized convection, Stephan et al. (2019b) also

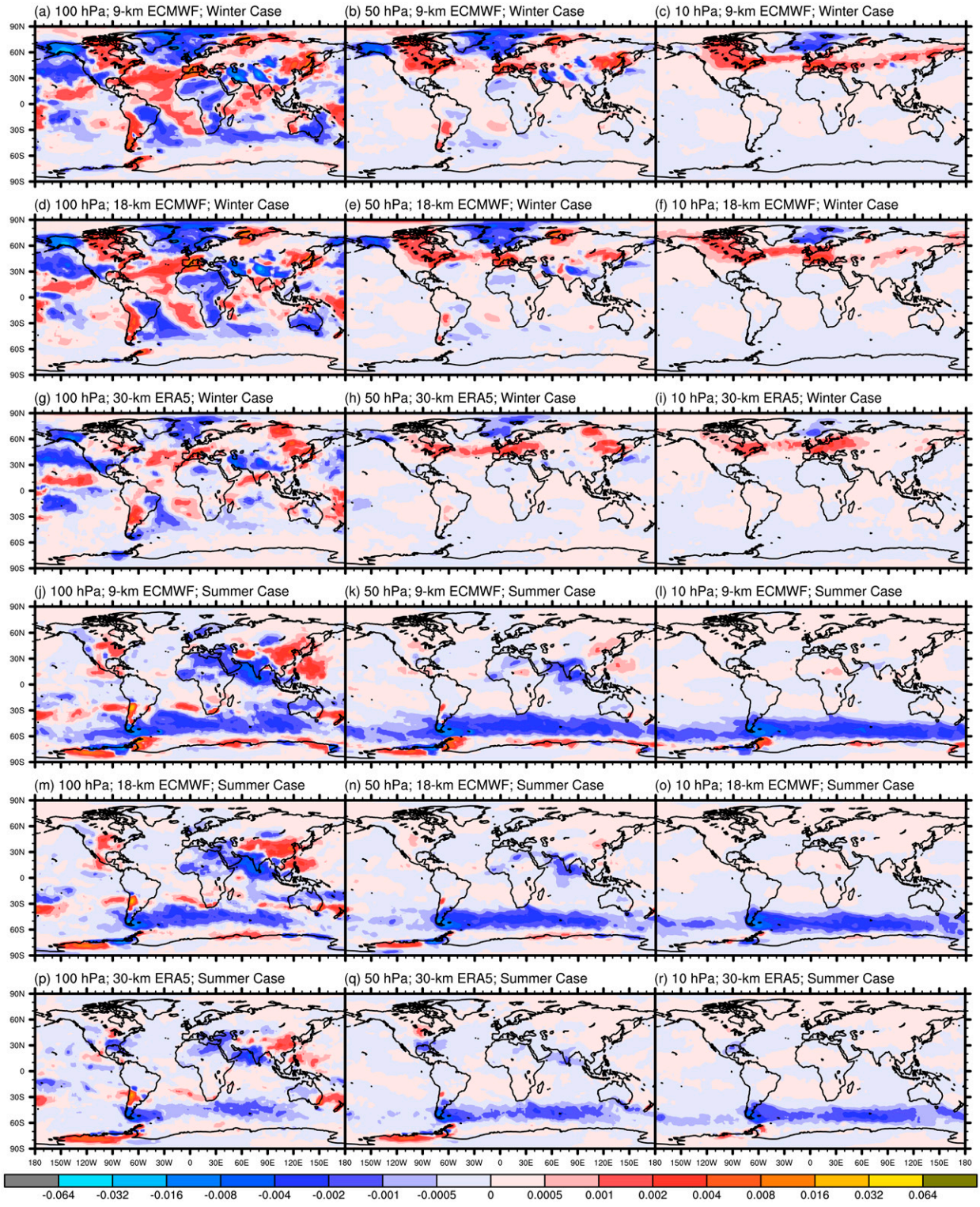

FIG. 4. As in Fig. 3, but for the global distributions of the 20-day mean meridional momentum flux per unit volume $\rho_0\overline{v'w'}$ (unit: Pa).

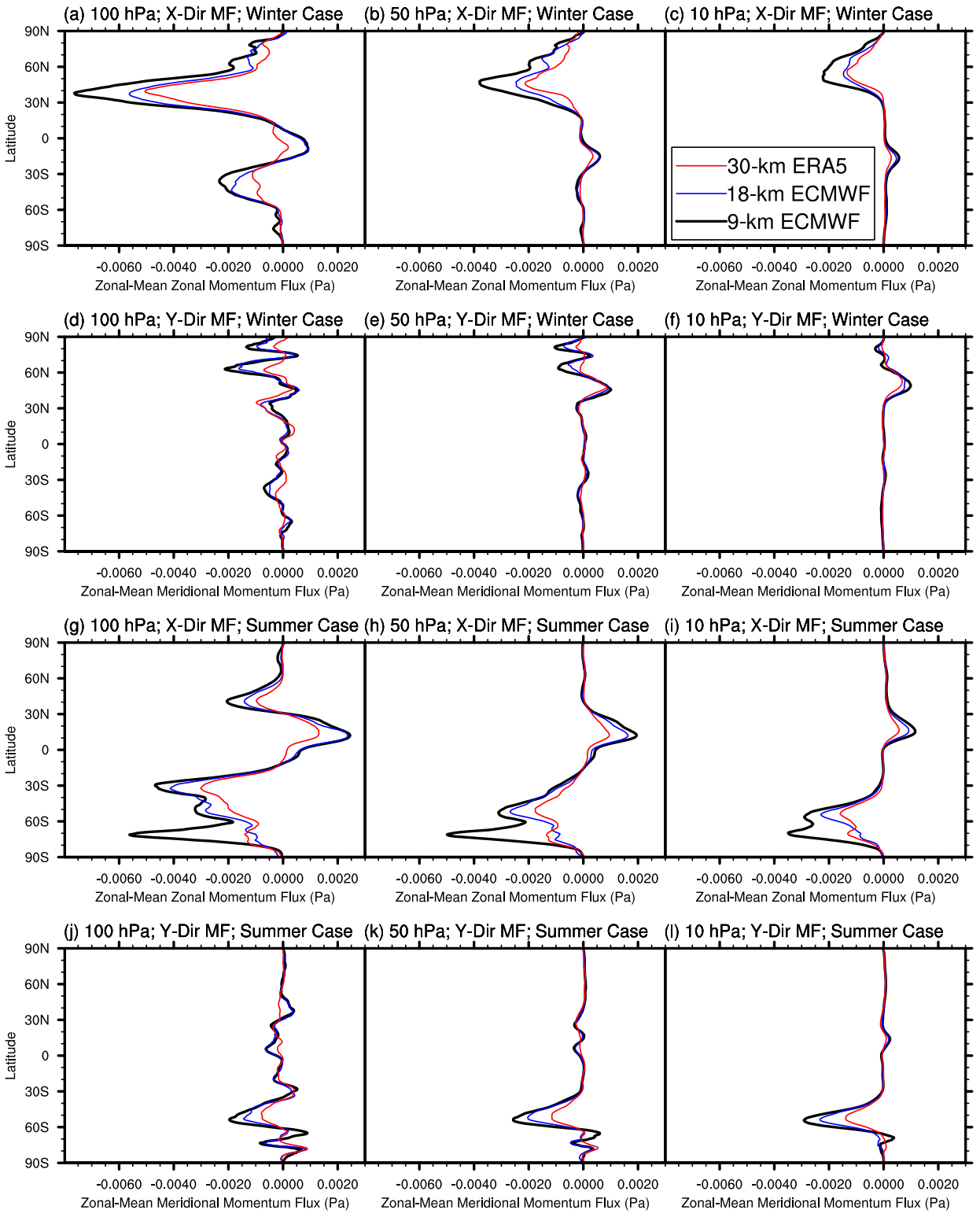

FIG. 5. The meridional profiles of (a)–(c),(g)–(i) the 20-day mean zonal-mean zonal momentum flux per unit volume $\rho_0\overline{u'w'}$ (unit: Pa) and (d)–(f),(j)–(l) the 20-day mean zonal-mean meridional momentum flux per unit volume $\rho_0\overline{v'w'}$ (unit: Pa) averaged for (a)–(f) the winter case and (g)–(l) the summer case at the three selected altitudes from stratosphere, including (left) 100, (center) 50, and (right) 10 hPa. Note that 100 hPa is loosely categorized into the group of the stratosphere in the current study. For comparison, three datasets with

demonstrated stronger updrafts in the upper troposphere, especially in the explicit simulation associated with more frequent heavy precipitation rates. Therefore, it is hypothesized that this asymmetric behavior could be due to the convective forcing rather than freely propagating gravity waves (see also Alexander et al. 2006), resulting in potential wave-induced flux calculation errors in the troposphere.

In contrast, the counterpart distribution in the stratosphere (Fig. 9) is highly symmetrical around zero, which is consistent with the basic assumption of freely propagating gravity waves. Note that the probability distribution of vertical motion has the widest spread at 10 hPa over the winter extratropics.

c. *Filtered results based on a simple method proposed in the current investigation*

To examine the above hypothesis in greater details, a simple filtering method is proposed in an attempt to eliminate the abovementioned asymmetry, with the aid of 12-h precipitation accumulation. Take the 9-km ECMWF IFS model again as an example, its original probability distributions (Fig. 8) are filtered based on two methods with different criteria, denoted as C1 and C2, respectively. Here, following ideas from Alexander et al. (2006), the C1 (C2) method neglects tropospheric perturbations (e.g., u', v', w') at any grid box with 12-h precipitation accumulation greater than 0.01 (0.001) m. To be more specific, the filtering procedure from Alexander et al. (2006) uses a height-dependent mask, applying $|w'| < w_{\max}(z)$ with an empirical profile $w_{\max}(z)$ chosen to be just larger than the largest free-wave perturbations at each height. Although justified in their study using simulations of deep convection over a very limited area, the above approach needs to be adapted to the high-resolution GCMs in the current study, which cover a wide variety of moist processes and background flows. Therefore, a simple solution for this adaption is provided here for the global datasets.

The corresponding filtered results are given in Fig. 10. Compared with Fig. 8 (first and third rows), the filtered distribution has become more symmetric with the additional procedure based on the C1 method (first and the third rows in Fig. 10). In particular, the asymmetric feature is reduced considerably at altitudes of 500 and 300 hPa, while the distribution at 200 hPa reaches an arguably acceptable symmetry. When further constraining the original distribution based on the C2 method with a lower threshold value associated with moisture, a high symmetry can be produced at all the above altitudes (second and fourth rows in Fig. 10), although the likelihood of over-filtering would increase in this case. The above analysis confirms the important role of moist processes in forcing strong updrafts with much higher frequency and ultimately forming the asymmetry in the troposphere. In addition, sensitivity tests have also been performed based on precipitation accumulation with shorter hours, as a mean to verify the validity of the proposed proposition. By proportionally scaling the threshold values in a similar way to the C1 and C2 methods, many important features in Fig. 10 can be reproduced. In sum, although the proposed approach is tentative, the current study shows promising and encouraging potential for adoption of information about moist processes such as precipitation accumulation to improve the accuracy of capturing the tropospheric-wave-induced perturbations.

The above findings provide considerable motivation for revisiting the tropospheric fluxes shown in Fig. 7. Figure 11 demonstrates the global distributions of the ratio between the filtered absolute momentum flux and the unfiltered one in Fig. 7. Despite the dominance of values close to one, the ratio distribution based on the C1 method (first and the third rows in Fig. 11) reveals several interesting spots with small values indicating a remarkable reduction in the filtered flux (e.g., South America in the winter case and Asia in the summer case), which are all traceable in the global map of the averaged 12-h precipitation accumulation (Fig. 1). Furthermore, the application of the C2 method (second and the fourth rows in Fig. 11) leads to much wider areas of low ratios expanded from the above spots. This large separation between two different calculations with and without the filtering method again supports the necessity of reducing the corresponding potential errors due to the convective forcing.

5. Comparison of absolute momentum flux between two different formulas

To further verify the reliability of the calculated absolute momentum flux per unit volume (M), this section compares its global distributions between two different approaches. The first approach, hereafter referred to as ORI, is calculated based on its original definition with the information of wind perturbations, the formula of which has been shown in Eq. (1). Here, M can be related to the absolute pseudo-momentum flux per unit volume (PM) in the below manner (Fritts and Alexander 2003; also read Wei et al. 2019 on the important role of M in gravity wave parameterization):

$$\mathrm{PM} = M\left(1 - \frac{f^2}{\Omega^2}\right), \tag{2}$$

where f is the Coriolis parameter and Ω is the intrinsic frequency. Following the ideas from Geller et al. (2013) on Eq. (2), the formula for M in the second approach, named the wind and temperature quadratics method (WTQ; also read Stephan et al. 2019a; Strube et al. 2021), can be obtained based on linear theory using the polarization relations for monochromatic

←
different resolutions are used in the calculations, including the 20-day control forecast by the operational 9-km ECMWF IFS model (IFS cycle 41R2, Tco1279) described in Zhang et al. (2019) (black line), that by the 18-km ECMWF IFS (IFS cycle 41R2, Tco639) (blue line), and the reanalysis datasets by the 30-km ERA5 (red line) (Hersbach et al. 2020).

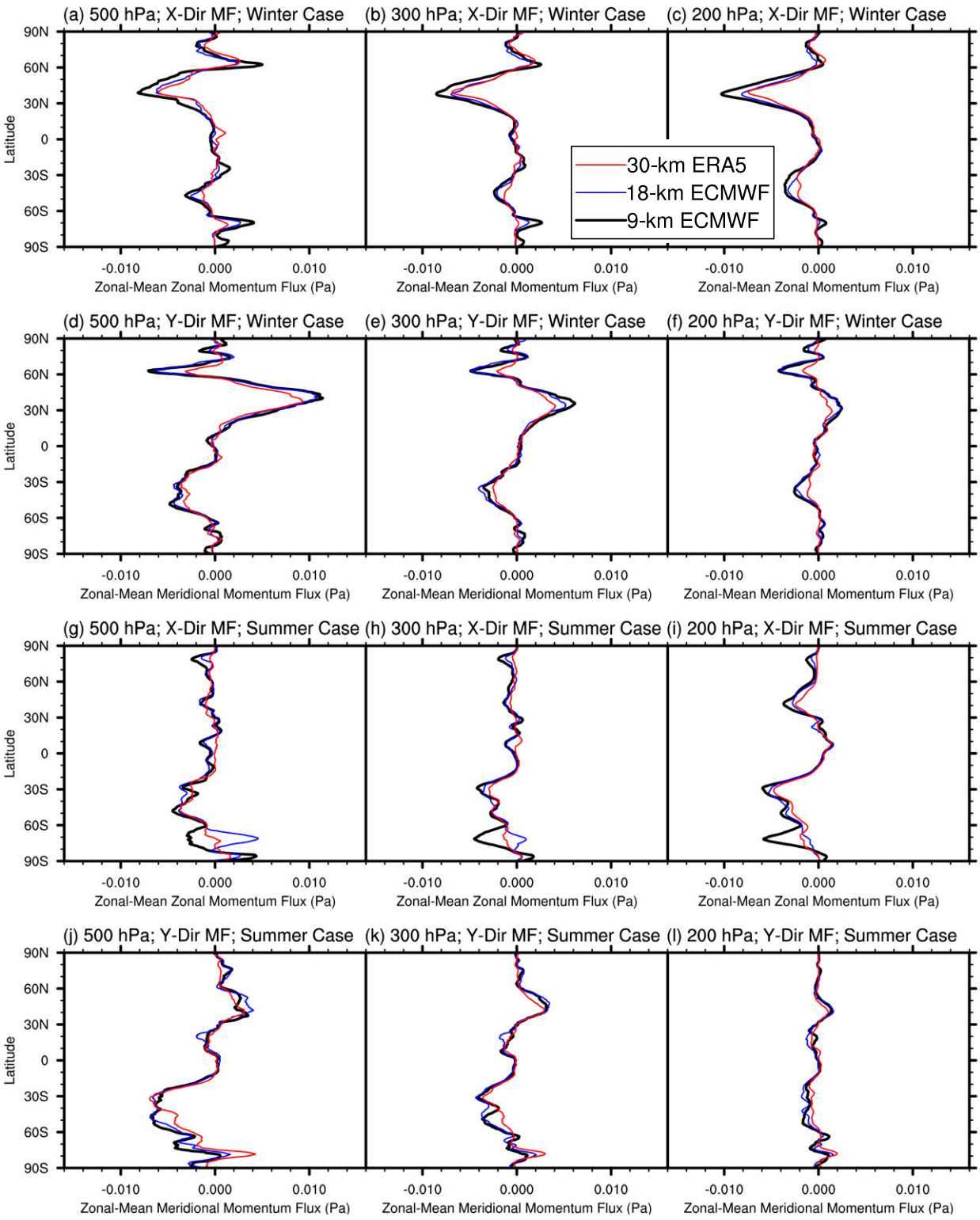

FIG. 6. As in Fig. 5, but for the three selected altitudes from troposphere, including (left) 500, (center) 300, and (right) 200 hPa.

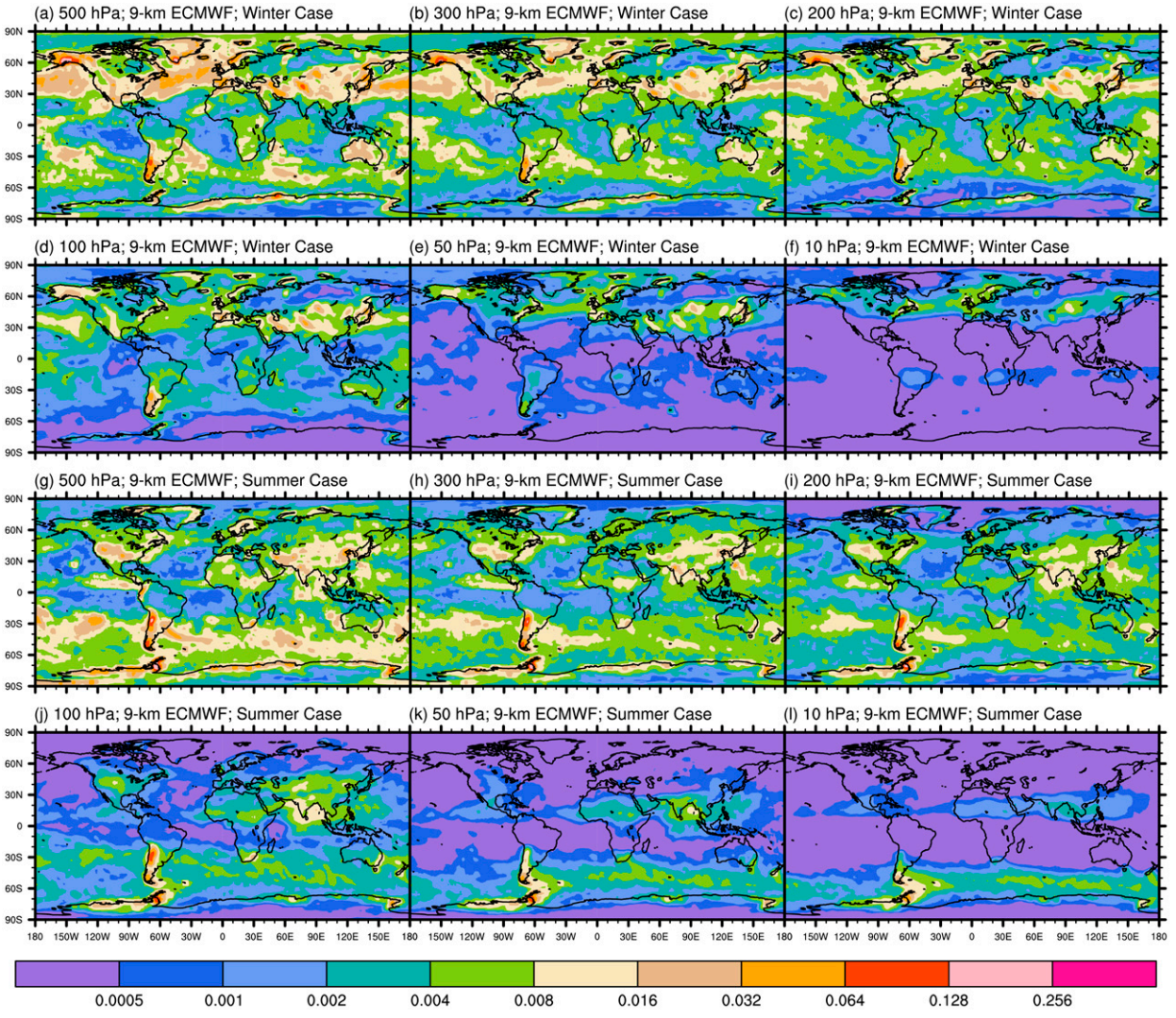

FIG. 7. The global distributions of the 20-day mean absolute momentum flux per unit volume (unit: Pa) averaged for (a)–(f) the winter case and (g)–(l) the summer case at the six selected altitudes from the troposphere and stratosphere, including (a),(g) 500; (b),(h) 300; (c),(i) 200; (d),(j) 100; (e),(k) 50; and (f),(l) 10 hPa. The calculations are based on the 20-day control forecast by the operational 9-km ECMWF IFS model (IFS cycle 41R2, Tco1279) described in Zhang et al. (2019).

gravity wave, which is shown as follows with the information of wind and temperature quadratics:

$$M = \sqrt{\rho_0^2 \overline{w'w'}\left(\overline{u'u'} + \overline{v'v'}\right)\left(1 + \frac{f^2}{\Omega^2}\right)^{-1}}, \qquad (3)$$

where $f^2/\Omega^2 = (fg/N^2)^2[\overline{(T'/T_0)^2}/\overline{(w'w')}]$. While ORI and WTQ should be identical for linear monochromatic gravity wave in theory, the equality is not self-evident in the current calculation approach or in other similar method, given that computation by ORI can result in gross underestimation (as also explained in Geller et al. 2013), due to cancellation of waves propagating toward opposite directions (i.e., east versus west and/or north versus south) in the overbar procedure for the averaging/smoothing step. In other words, in general it is expected that WTQ > ORI, unless $u'w'$ and $v'w'$ averaged within the overbar are both mono-signed. Nonetheless, questions still remain about their quantitative comparison in both the troposphere and the stratosphere.

On one hand, to investigate the above comparison in the troposphere, Fig. 12 illustrates the global distributions for the ratio of M between the WTQ approach and the ORI approach in both selected periods, using the filtering methods with criteria introduced in section 4c. For the ratio distribution based on the C1 method (first and the third rows in Fig. 12), areas with high ratios, revealing a large separation between those two approaches with WTQ being much greater than ORI, can be identified over the tropics. Interestingly, the application of the C2 method (second and the fourth rows in Fig. 12) results in a remarkable reduction of those high ratios. This

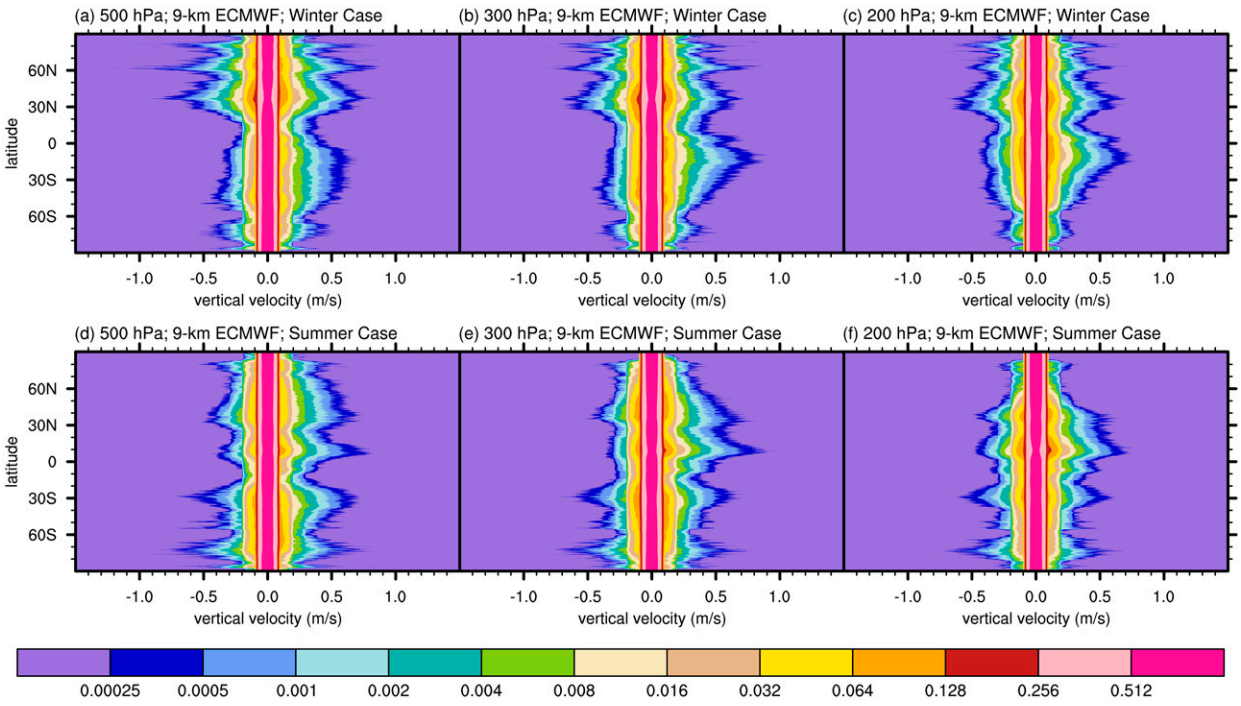

FIG. 8. The probability distributions of the vertical motion perturbation for (a)–(c) the winter case and (d)–(f) the summer case at the three selected altitudes from troposphere, including (left) 500, (center) 300, and (right) 200 hPa. The calculations are based on the 20-day control forecast by the operational 9-km ECMWF IFS model (IFS cycle 41R2, Tco1279) described in Zhang et al. (2019).

finding, in addition to its comparison with the unfiltered ratio map in the troposphere (not shown), again suggests that the filtering methods could help to eliminate the potential small-scale perturbations due to convective forcing, better highlighting linear monochromatic gravity wave signals. Furthermore, it is also implied by Fig. 12 that sources like convection in the tropics, with clear signals indicating WTQ > ORI, tend to generate waves propagating in all directions [which lead to gross underestimation by the ORI approach, as explained in Geller et al. (2013)], in contrast to other sources (e.g., topography and jet–front systems) in the middle latitudes. In addition, non-monochromatic waves with different ranges of frequencies, creating cross terms that may not be negligible in the tropics, could also bring about the separation between WTQ and ORI.

On the other hand, in comparison with the above discussion on the troposphere, Fig. 13 demonstrates the corresponding stratospheric ratio map without using any filtering method. Unlike in the troposphere, this stratospheric ratio map is more dominated by values much closer to one, with relatively limited areas of values over three. Nonetheless, it is still in general expected that WTQ > ORI, as confirmed and quantified in Figs. 12 and 13. Besides, as shown in Koshyk and Hamilton (2001) and Callies et al. (2016) and reemphasized in Stephan et al. (2019a), the spectral separation between wave motion and geostrophic motion is rather distinct in the stratosphere, especially compared with the troposphere. Therefore, the current calculation for the wave-induced fluxes, despite a lack of any filtering method, is justified in the stratosphere.

6. Discussion and conclusions

Consistent with the previous studies (e.g., Chun et al. 2019; Hindley et al. 2020), stratospheric momentum fluxes resolved by the 9-km ECMWF IFS model are characterized by 1) westward fluxes in the winter extratropics, 2) eastward fluxes in the summer tropics, and 3) meridional convergence into the winter jet. Note that such a dominance of the above westward fluxes is consistent with Wei et al. (2016) based on an ensemble of high-resolution idealized moist baroclinic jet–front systems. Also, this investigation resembles other studies based on the global convection-permitting models (e.g., Holt et al. 2017; Stephan et al. 2019a), such as the locally enhanced gravity wave activity signals near the southern tip of the Andes and near the Antarctic Peninsula during the austral winter. In contrast, the corresponding stratospheric mean meridional momentum fluxes, which can be locally as important as the above zonal counterpart, show different behaviors of global distribution characteristics, with northward and southward momentum fluxes alternating with each other especially at the lower altitude. This banding could be related to bands of gravity wave sources from which the waves propagate north and south on either side of the source band, in addition to the effects by the background during propagation (e.g., Fig. 2). The above general patterns from the zonal and meridional momentum fluxes, as well as their dramatically weakening

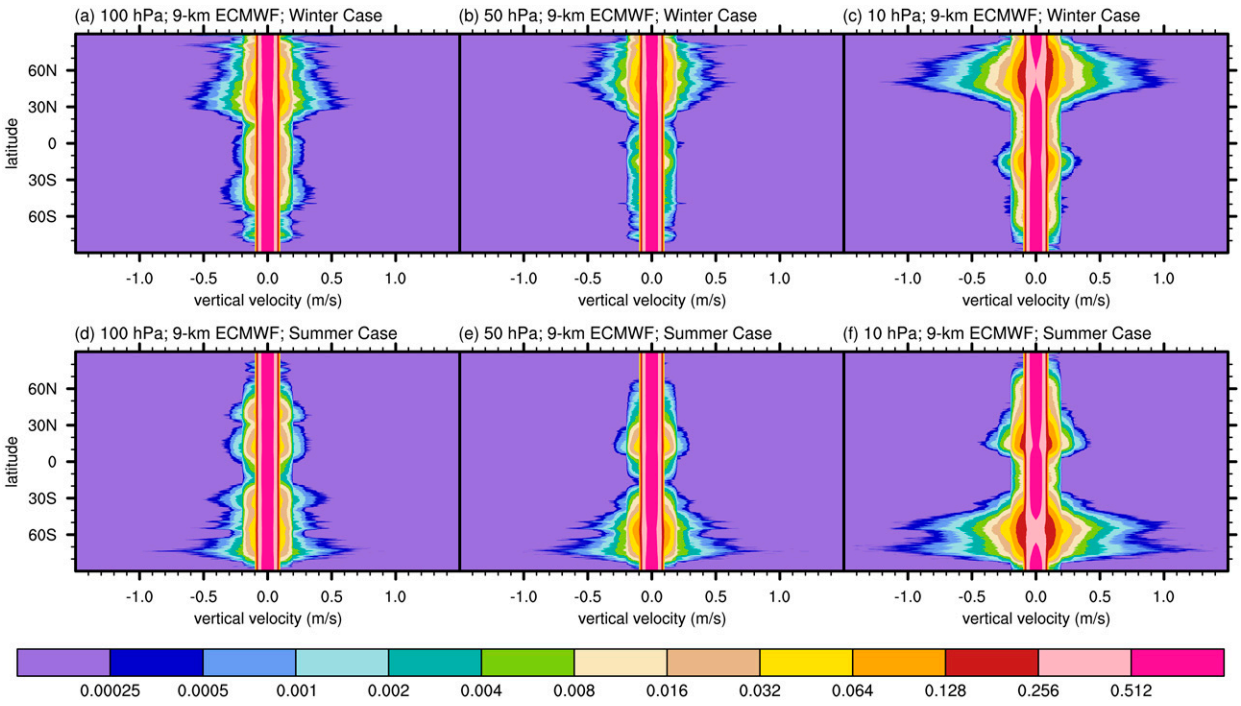

FIG. 9. As in Fig. 8, but at the three selected altitudes from stratosphere, including (left) 100, (center) 50, and (right) 10 hPa.

signals with height, can also be found in the 18-km ECMWF IFS model and the 30-km ERA5 datasets. However, both events illustrate conclusive evidence that the ECMWF datasets with coarser resolution correspond to weaker signals of the stratospheric momentum fluxes in general, regardless of whether regridding is applied (also read appendix section e). Nonetheless, ERA5 has been an important source for climatological studies of gravity waves over many years.

In contrast to the stratosphere, the tropospheric small-scale perturbations can be relatively noisy for gravity wave analysis, due to convective forcing (Alexander et al. 2006). Therefore, a simple filtering method, which neglects the tropospheric short-scale perturbation at any model grid box with 12-h precipitation accumulation greater than a chosen threshold value, is proposed in an attempt to efficiently minimize such errors in high-resolution global datasets. It can be shown that the filtered distribution has become more symmetric with the additional proposed procedure. In addition, the application of the filtering method could lead to a remarkable reduction of the tropospheric absolute momentum flux estimations, further supporting the necessity of reducing the corresponding errors due to convective forcing.

This paper also demonstrates the comparison of the estimated absolute momentum flux between two different formulas, which should be, in theory, identical for linear monochromatic gravity waves with mono-signed fluxes. In the troposphere, areas associated with large separations between those two approaches can be identified. Interestingly, the application of the filtering method results in a remarkable reduction of those separations, suggesting again that the filtering method could help to eliminate uncertainties due to convective forcing, better highlighting linear monochromatic gravity wave signals. In the stratosphere, the WTQ approach is more similar to the ORI approach. A probable explanation for this transition behavior is that the zonal wind shear in the stratosphere tends to selectively remove eastward- or westward-propagating gravity waves, consequently leading to much less cancellation of positive/negative fluxes for the $\overline{u'w'}$ term. In comparison, the meridional wind shear is likely to be relatively small or more random, so the north–south cancellation might remain similar in the stratosphere as it is in the troposphere. Nonetheless, it is still in general expected that WTQ > ORI, as confirmed and quantified in both troposphere and stratosphere. Furthermore, note that Stephan et al. (2019a) also found a very good qualitative agreement for the computation of the stratospheric fluxes between two very different methods (i.e., their S3D approach, which is based on only the temperature field and focuses on the dominant wave versus their WTQ approach which is based on temperatures and three-dimensional winds).

To conclude the current study, an update to Fig. 7 for the computation of absolute gravity wave momentum flux is produced in Fig. 14 as a finale to this paper, with two upgraded modifications. First, in order to avoid the gross underestimation by the ORI approach in both troposphere and stratosphere (Geller et al. 2013), the WTQ approach is adopted. Second, in an attempt to eliminate the short-scale perturbations by convective forcing (Alexander et al. 2006), the C1 filtering method, which has already resulted in a relatively reasonable feature of symmetry in the probability distribution, is applied for the computation of tropospheric fluxes.

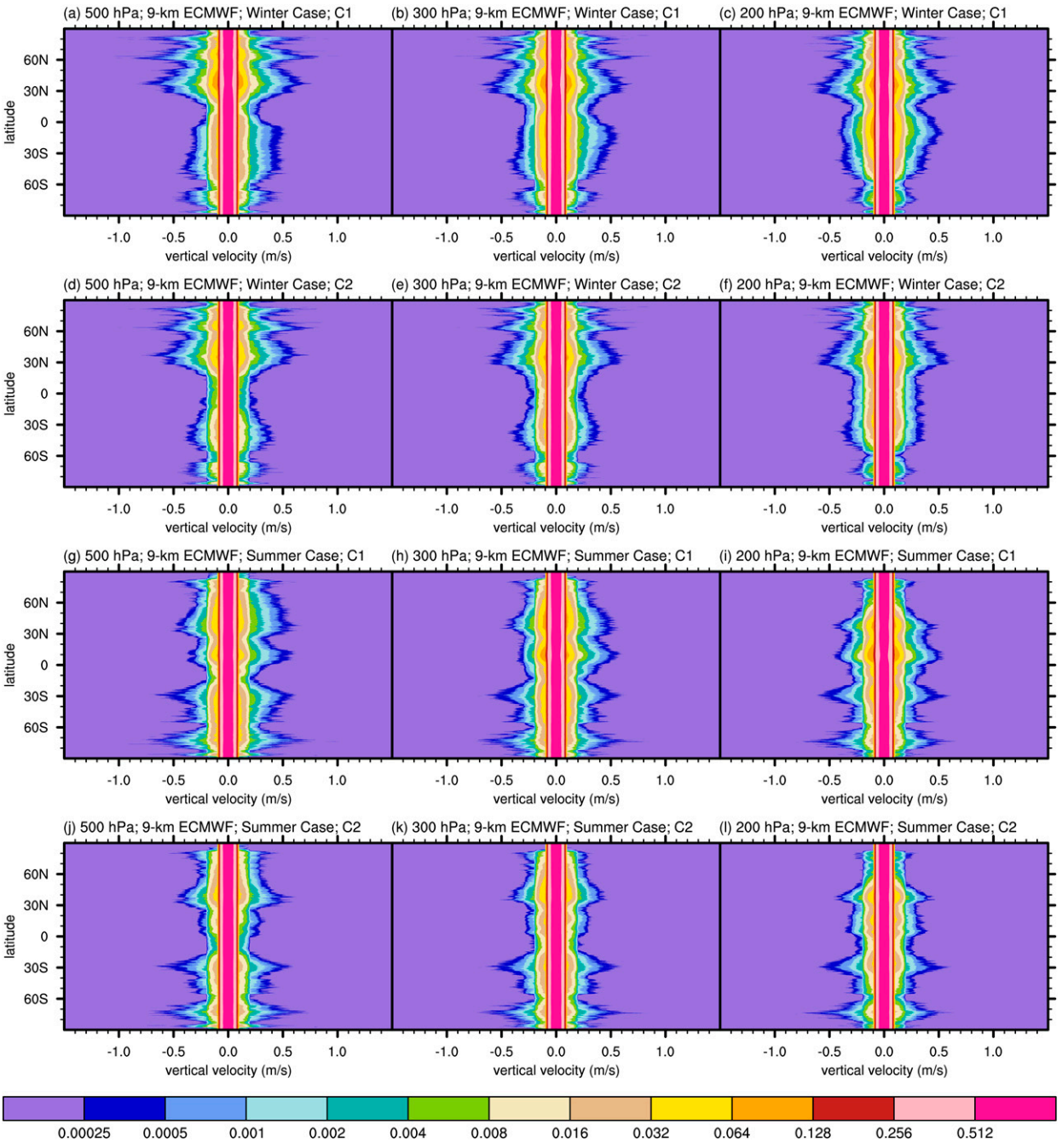

FIG. 10. The corrected probability distributions of the vertical motion perturbation along the meridional direction for (a)–(f) the winter case and (g)–(l) the summer case at the three selected altitudes from the troposphere, including (left) 500, (center) 300, and (right) 200 hPa. This plot compares two correction methods for eliminating the tropospheric vertical motion perturbation potentially by the convective forcing based on the 12-h precipitation accumulation, including (a)–(c),(g)–(i) the C1 method and (d)–(f),(j)–(l) the C2 method described in section 4c. The calculations are based on the 20-day control forecast by the operational 9-km ECMWF IFS model (IFS cycle 41R2, Tco1279) described in Zhang et al. (2019).

Note that the likelihood of over-filtering would increase when using the C2 method, in contrast to the C1 method. Overall, fluxes in Fig. 14 are notably stronger than those in Fig. 7, due to the first modification. After using the divergent wind component and the C1 filtering method, the vertical variations of the tropospheric signals are effectively weakened (also read appendix section d), especially compared with the tendency of continuously decreasing fluxes in the stratosphere.

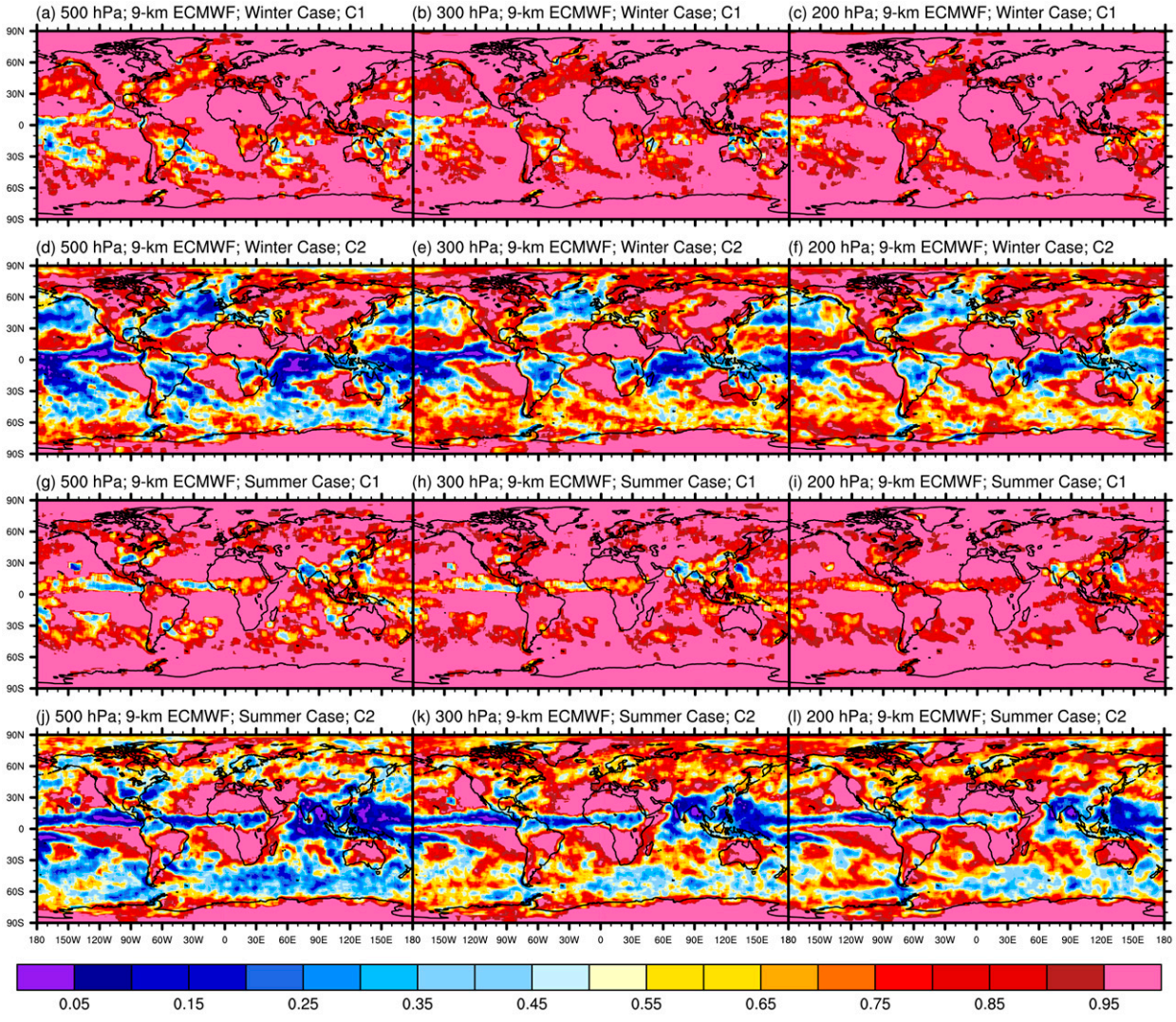

FIG. 11. The global distributions of the ratio (unitless) between two different calculations of the 20-day mean absolute momentum flux per unit volume with and without the correction method for (a)–(f) the winter case and (g)–(l) the summer case at the three selected altitudes from troposphere, including (left) 500, (center) 300, and (right) 200 hPa. This plot compares two correction methods for eliminating the tropospheric perturbations potentially by the convective forcing based on the 12-h precipitation accumulation, including (a)–(c),(g)–(i) the C1 method and (d)–(f),(j)–(l) the C2 method described in section 4c. The calculations are based on the 20-day control forecast by the operational 9-km ECMWF IFS model (IFS cycle 41R2, Tco1279) described in Zhang et al. (2019).

Compared with the parameterization study in Bushell et al. (2015; e.g., their Fig. 13), a broad consistency can be identified at the lower stratosphere, but fluxes reduce more dramatically toward the middle stratosphere in the 9-km experiments (also read Fig. 3 in Geller et al. 2013). Furthermore, noticeable fluxes are still sustained at high latitudes near the poles in the troposphere, in contrast to the stratosphere (also read Fig. 2 in Geller et al. 2013). Those findings, including their corresponding zonal-mean distributions in Fig. S11 in the online supplemental material, are worth further assessment in the future, with collaborative efforts from modeling and observations.

There are several limitations that need to be clarified in the current paper. First, questions remain about its accuracy in terms of capturing the tropospheric wave-induced perturbations, as well as how to determine the threshold values under different flow regimes with varying moist conditions. This could be verified in the future project, based on the high-resolution idealized simulations (e.g., experiments of moist baroclinic jet–front systems and/or localized convection; Wei and Zhang 2014; Sun et al. 2017) with model output at much higher temporal frequencies. Second, a comprehensive survey on the sensitivities of the resolved flux calculations to different choices among numerous existing

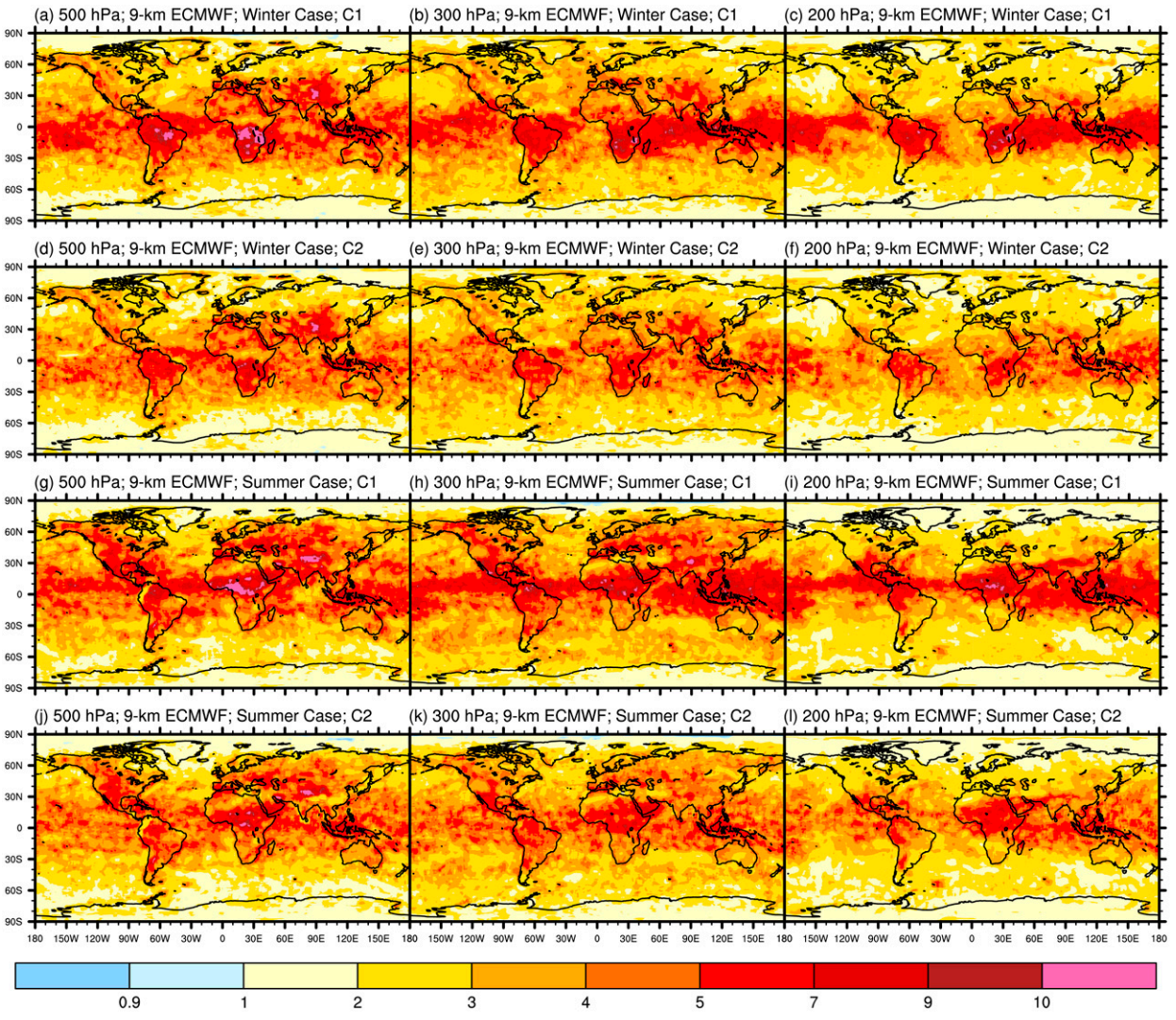

FIG. 12. The global distributions of the ratio (unitless) between two different calculations of the 20-day mean absolute momentum flux per unit volume based on the WTQ approach and based on the ORI approach for (a)–(f) the winter case and (g)–(l) the summer case at the three selected altitudes from troposphere, including (left) 500, (center) 300, and (right) 200 hPa. This plot compares two correction methods for eliminating the tropospheric perturbations potentially by the convective forcing based on the 12-h precipitation accumulation, including (a)–(c),(g)–(i) the C1 method and (d)–(f),(j)–(l) the C2 method described in section 4c. The calculations are based on the 20-day control forecast by the operational 9-km ECMWF IFS model (IFS cycle 41R2, Tco1279) described in Zhang et al. (2019).

methods (e.g., Žagar et al. 2015b, 2017; Stephan et al. 2019a,b, 2020; articles introduced in section 2d) is also worth conducting. Third, studies have suggested that the resolved gravity wave momentum fluxes can continue to increase if the horizontal resolution in the ECMWF IFS model is further increased from 9 km (e.g., Stephan et al. 2019a; Wedi et al. 2020; Polichtchouk et al. 2022). Therefore, evaluations are needed to better understand the sensitivity to the enhanced model resolution, especially in view of validating the simulated gravity waves compared with the most advanced measurements, cutting-edge parameterizations, and other state-of-the-art high-resolution GCMs (e.g., Geller et al. 2013).

Nonetheless, many interesting results from this study (e.g., Figs. 14 and S11) offer potential to gain a deeper understanding on gravity wave dynamics and its global impact. Those promising and encouraging findings provide considerable motivation for our next steps on this research topic.

Acknowledgments. Junhong Wei was supported by the National Natural Science Foundation of China (Grant 42075005), Guangdong Province Key Laboratory for Climate Change and Natural Disaster Studies (Grant 2020B1212060025), and the Innovation Group Project of Southern Marine Science and Engineering Guangdong Laboratory (Zhuhai) (Grant 311021001). Fuqing Zhang was supported by the National

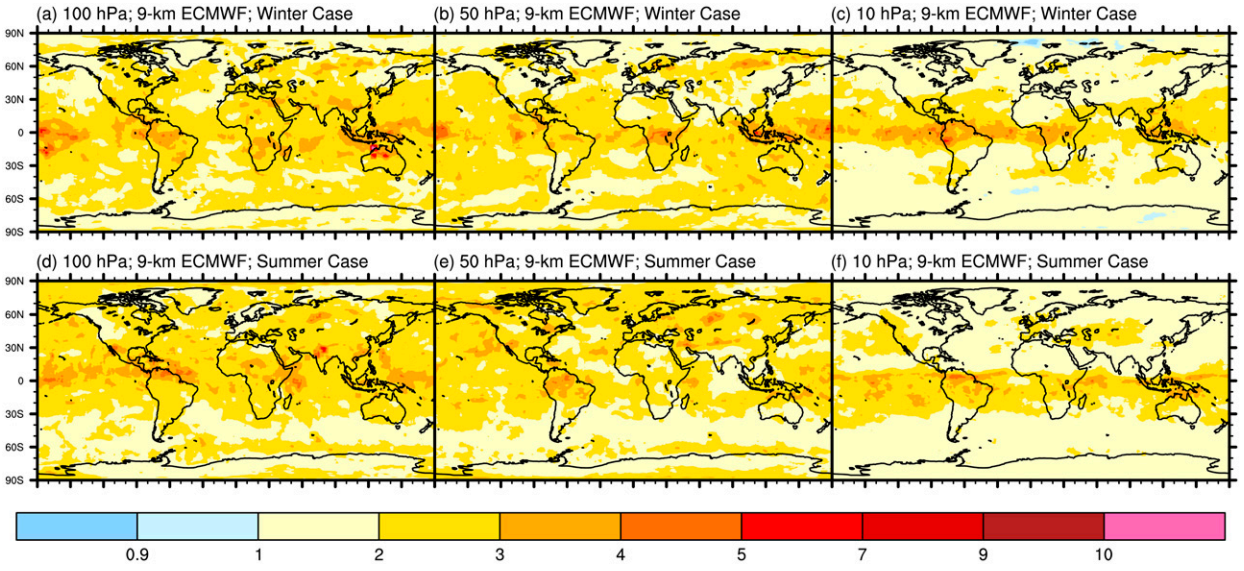

FIG. 13. The global distributions of the ratio (unitless) between two different calculations of the 20-day mean absolute momentum flux per unit volume based on the WTQ approach and based on the ORI approach for (a)–(c) the winter case and (d)–(f) the summer case at the three selected altitudes from stratosphere, including (left) 100, (center) 50, and (right) 10 hPa. Note that 100 hPa is loosely categorized into the group of the stratosphere in the current study. The calculations are based on the 20-day control forecast by the operational 9-km ECMWF IFS model (IFS cycle 41R2, Tco1279) described in Zhang et al. (2019).

Science Foundation through Grant 1712290. Jadwiga H. Richter was supported by the National Center for Atmospheric Research (NCAR), which is a major facility sponsored by the National Science Foundation (NSF) under Cooperative Agreement 1852977. M. Joan Alexander was supported by the National Science Foundation through Grant 1829373. Y. Qiang Sun was supported by Award NA18OAR4320123 from the National Oceanic and Atmospheric Administration, U.S. Department of Commerce. We are very grateful for the discussions with Julio Bacmeister, Rolando Garcia, Christopher G. Kruse, Linus Magnusson, Inna Polichtchouk, Richard Rotunno, Claudia Christine Stephan, and Anne K. Smith. We acknowledge the Texas Advanced Computing Center (TACC) at the University of Texas at Austin (http://www.tacc.utexas.edu) for the computational resources invoked in this research. We also benefited from the insightful comments from three anonymous reviewers on an earlier version of the manuscript.

APPENDIX

Additional Details on Gravity Wave Momentum Flux Computation

In the current study, the computations of the resolved wave-induced fluxes have been performed individually for each available instantaneous model output as many other studies (e.g., Geller et al. 2013; Holt et al. 2017; Stephan et al. 2019a; Chun et al. 2019). A brief introduction to the computation method used for this work is shown in section 2. In this appendix, additional details on gravity wave momentum flux computation are documented.

a. Decomposition of the winds into rotational and divergent components

In the current study, the divergent components of the winds (also read Žagar et al. 2015a; Bierdel et al. 2016; Sun et al. 2017) are extracted by the Helmholtz decomposition technique, before any spatial filtering/smoothing method is applied. To investigate the sensitivity of the flux estimations to this particular procedure, Figs. S1 and S2 demonstrate the comparison of absolute momentum fluxes between using the full winds (i.e., the sum of rotational and divergent components) and using only the divergent wind components for the winter case and the summer case, respectively. In the stratosphere, the flux distributions based on the full winds are essentially identical to those based on the divergent wind components (the second and the fourth rows in Figs. S1 and S2). However, the tropospheric fluxes with using the full winds are noticeably stronger than those with using only the divergent wind components (the first row versus the third row in Figs. S1 and S2). Furthermore, the abovementioned tropospheric differences are also identified in other datasets used in the current work (not shown), regardless of whether regridding is applied (also read appendix section e). Therefore, in order to better focus on the unbalanced gravity wave dynamics, all the results on the flux estimations in this article are obtained with using only the divergent wind components in both stratosphere and troposphere, so that the balanced components of winds are largely eliminated.

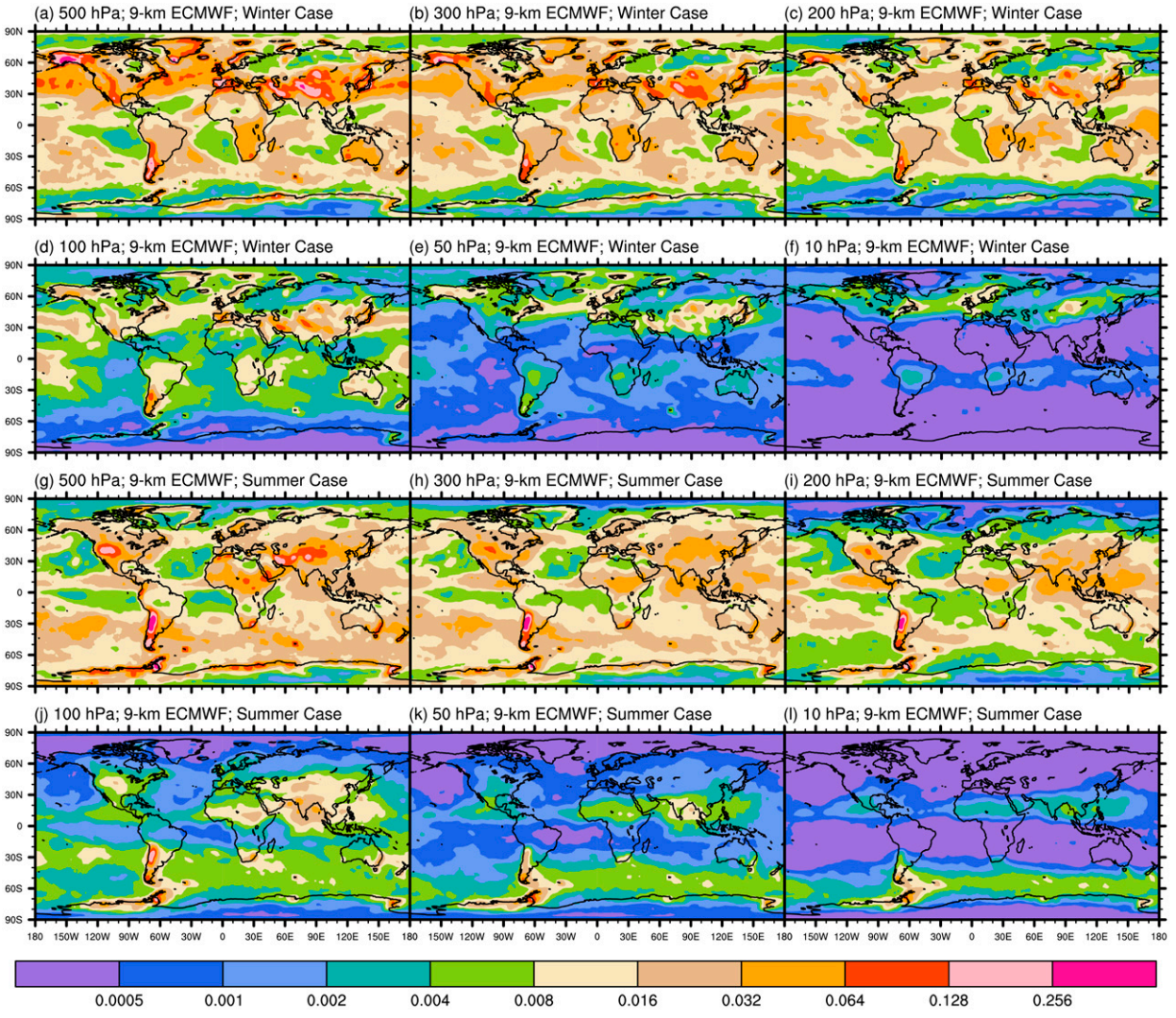

FIG. 14. As in Fig. 7, but for the following two aspects. First, the WTQ method is applied for the computation of absolute momentum flux per unit volume (unit: Pa), instead of the ORI method. Second, the C1 filtering approach is applied for the computation of tropospheric fluxes. The corresponding zonal-mean results are shown in Fig. S11.

b. Methodology to retrieve the large-scale background flows and the short-scale perturbations

As discussed in section 4b, there are two important steps that require the computation for the overline, and the first step is to retrieve the large-scale background flows (e.g., $\overline{u}$) and the short-scale perturbations (e.g., $u' = u - \overline{u}$). This part of the appendix compares three commonly used approaches in the global datasets for this particular first step, which are described as below.

(i) The computation for the overline is defined as the $5^\circ \times 5^\circ$ latitude–longitude horizontal running average. This method follows the main ideas of the literature from Kim and Chun (2010), Kim et al. (2012), Chun et al. (2019), and so on.

(ii) The computation for the overline is defined as the zonal retrieval of all zonal wavenumbers equal to or less than 72 at each available latitude. This method follows the main ideas of the literature from Stephan et al. (2019a), Gupta et al. (2021), and so on. Note that cutoff wavenumbers 12 and 20 are used in those two articles, respectively.

(iii) The computation for the overline is defined as the spectrally truncated retrieval of total wavenumbers equal to or less than 40 in the spherical harmonic expansion. This method follows the main ideas of the literature from Geller et al. (2013), Wedi et al. (2020), and so on.

An extensive survey has been conducted to investigate the sensitivities of the resolved flux calculations to different available choices, before the third approach is adopted as the methodology to retrieve the large-scale background flows. Based on the current survey on the comparison among the above three approaches, the salient features of the extracted short-scale

perturbations and the resulting fluxes are broadly consistent with each other, which confirms that the main conclusion should be insensitive to the choice among the above three background retrieval methodologies. With that being said, very minor differences of the calculated resolved fluxes can still be identified (e.g., regions near the poles), especially with the third method exhibiting the strongest signal in general. This discrepancy, as exemplified by the comparison between Fig. 3 and Fig. S3, should be expected, since the first two approaches tend to filter much smaller zonal wavelengths at higher latitudes than at lower latitudes. Therefore, the third approach is employed for the first step of the overline computation, due to its superiority in processing signals over high latitudes. In addition to that, we have also further investigated the sensitivities of the flux estimations to changing the selected cutoff wavenumbers by ±4, which in the end do not affect the main results.

c. Methodology to obtain the smoothing of the quadratic quantities

As discussed in section 4b, there are two important steps that require the computation for the overline, and the second step is to obtain the smoothing of the quadratic quantities (e.g., from $u'w'$ to $\overline{u'w'}$). Following the previous part of the appendix, this part further compares the three commonly used approaches in the global datasets, for this particular second step.

Many major conclusions are, once again, consistent with each other among the three approaches introduced in the previous part. For example, all the approaches continue to show that stronger fluxes are found in the ECMWF forecast with finer resolution, and that ERA5 datasets have the weakest signals in general. This is still the case even after interpolating all the datasets into the same horizontal grid (also read appendix section e). However, there is one notable issue in the spatial filter with a specific cutoff wavenumber (i.e., the second and the third approaches), when computing the smoothing of the quadratic quantities. As exemplified in Fig. S4, spurious ripple patterns in the flux distributions can be identified in the Southern Hemisphere. Those issues are commonly seen from the field with sharp and narrow edges (which is often the case in the lower stratosphere and in the troposphere), as they tend to affect a wide range of wavenumber spectrum. Based on the above findings, the first approach is employed for the second step of the overline computation, despite the fact that many major results (e.g., the comparison of zonally averaged directional fluxes among various datasets) are consistent with each other among different approaches.

d. Vertical variations of the tropospheric flux distribution with different approaches

To investigate the vertical variation of the flux distribution with different approaches, Figs. S5 and S6 compare the tropospheric results among (i) using full winds, (ii) using only the divergent wind components, (iii) using the divergent wind component and the C1 filtering method, and (iv) using the divergent wind component and the C2 filtering method for the winter case and the summer case, respectively. It can be shown from the results based on the full winds that the flux signals dramatically decrease with height. However, after updating all the flux computations with using only the divergent wind components, the abovementioned decreasing feature has been largely reduced. Moreover, the C1 and C2 filtering methods proposed in the current article also appear to further weaken the tendency of those decreasing behaviors with height.

It should be kept in mind that the assumption of the dominance by the upward-only gravity wave propagation may not be valid in the troposphere, unlike what is often applied in the middle atmosphere by many gravity wave parameterization schemes (Plougonven et al. 2020). For example, the tropopause is often considered as a (partial) reflector for wave propagation (Lindzen and Tung 1976; Lane and Zhang 2011). Besides, downward-propagating gravity waves are also known to occur in the vicinity of unbalanced upper-tropospheric jet streaks (Uccellini and Koch 1987; Plougonven and Zhang 2014). This may serve as a candidate explanation for the abovementioned weak decreasing behaviors in the troposphere.

e. Sensitivity of flux comparison among datasets to regridding

Tests have also been performed in order to further understand the effects of model resolution. For better comparison, high-resolution global datasets are interpolated to the same horizontal grid before the analysis. With this procedure, three additional groups of regridded datasets are generated, including:

(i) 9kmEC_18km: the 9-km ECMWF IFS experiment interpolated to the same horizontal grid of the 18-km ECMWF IFS experiment;
(ii) 9kmEC_30km: the 9-km ECMWF IFS experiment interpolated to the same horizontal grid of the 30-km ERA5 dataset;
(iii) 18kmEC_30km: the 18-km ECMWF IFS experiment interpolated to the same horizontal grid of the 30-km ERA5 dataset.

Take the stratospheric zonal momentum flux global distributions as an example, Figs. S7 and S8 demonstrates their comparison among the three un-regridded datasets (top three panels) and the abovementioned three regridded datasets (lower three panels) for the winter case and the summer case, respectively. Furthermore, Figs. S9 and S10 also illustrate the comparison of the zonally averaged directional fluxes in the stratosphere and in the troposphere, respectively. Based on those analyses, the additional computations continue to support the statement that stronger stratospheric fluxes are found in the ECMWF forecast with finer resolution, and that ERA5 datasets have the weakest signals in general, regardless of whether regridding is applied. To be more specific, Fig. S9 illustrates that the regridded flux distribution from 9kmEC_18km is almost

identical to the un-regridded counterpart. Further coarsening the datasets to 9kmEC_30km appears to result in a very minor decrease in the flux signals, but they are still stronger than the 18-km ECMWF IFS experiment and the 30-km ERA5 datasets. In addition to that, no apparent difference is found between the 18kmEC_30km and its un-regridded counterpart. Similar comparison between regridded datasets and their un-regridded counterparts is also identified in the troposphere.

REFERENCES

Alexander, M. J., and T. J. Dunkerton, 1999: A spectral parameterization of mean-flow forcing due to breaking gravity waves. *J. Atmos. Sci.*, **56**, 4167–4182, https://doi.org/10.1175/1520-0469(1999)056<4167:ASPOMF>2.0.CO;2.

——, J. H. Richter, and B. R. Sutherland, 2006: Generation and trapping of gravity waves from convection with comparison to parameterization. *J. Atmos. Sci.*, **63**, 2963–2977, https://doi.org/10.1175/JAS3792.1.

——, and Coauthors, 2010: Recent developments in gravity-wave effects in climate models and the global distribution of gravity-wave momentum flux from observations and models. *Quart. J. Roy. Meteor. Soc.*, **136**, 1103–1124, https://doi.org/10.1002/qj.637.

Andrews, D., J. Holton, and C. Leovy, 1987: *Middle Atmosphere Dynamics*. International Geophysics Series, Vol. 40, Academic Press, 489 pp.

Bauer, P., A. Thorpe, and G. Brunet, 2015: The quiet revolution of numerical weather prediction. *Nature*, **525**, 47–55, https://doi.org/10.1038/nature14956.

——, P. D. Dueben, T. Hoefler, T. Quintino, T. C. Schulthess, and N. P. Wedi, 2021: The digital revolution of Earth-system science. *Nat. Comput. Sci.*, **1**, 104–113, https://doi.org/10.1038/s43588-021-00023-0.

Bechtold, P., M. Köhler, T. Jung, F. Doblas-Reyes, M. Leutbecher, M. Rodwell, F. Vitart, and G. Balsamo, 2008: Advances in simulating atmospheric variability with the ECMWF model: From synoptic to decadal time-scales. *Quart. J. Roy. Meteor. Soc.*, **134**, 1337–1351, https://doi.org/10.1002/qj.289.

Becker, E., and S. Vadas, 2018: Secondary gravity waves in the winter mesosphere: Results from a high-resolution global circulation model. *J. Geophys. Res. Atmos.*, **123**, 2605–2627, https://doi.org/10.1002/2017JD027460.

Bierdel, L., C. Snyder, S. Park, and W. C. Skamarock, 2016: Accuracy of rotational and divergent kinetic energy spectra diagnosed from flight-track winds. *J. Atmos. Sci.*, **73**, 3273–3286, https://doi.org/10.1175/JAS-D-16-0040.1.

——, T. Selz, and G. C. Craig, 2018: Theoretical aspects of upscale error growth on the mesoscales: Idealised numerical simulations. *Quart. J. Roy. Meteor. Soc.*, **144**, 682–694, https://doi.org/10.1002/qj.3236.

Blunden, J., and D. S. Arndt, 2016: State of the Climate in 2015. *Bull. Amer. Meteor. Soc.*, **97** (8), Si–S275, https://doi.org/10.1175/2016BAMSStateoftheClimate.1.

Bölöni, G., B. Ribstein, J. Muraschko, C. Sgoff, J. Wei, and U. Achatz, 2016: The interaction between atmospheric gravity waves and large-scale flows: An efficient description beyond the nonacceleration paradigm. *J. Atmos. Sci.*, **73**, 4833–4852, https://doi.org/10.1175/JAS-D-16-0069.1.

Bossert, K., S. L. Vadas, L. Hoffmann, E. Becker, V. L. Harvey, and M. Bramberger, 2020: Observations of stratospheric gravity waves over Europe on 12 January 2016: The role of the polar night jet. *J. Geophys. Res. Atmos.*, **125**, e2020JD032893, https://doi.org/10.1029/2020JD032893.

Bramberger, M., A. Dörnbrack, H. Wilms, S. Gemsa, K. Raynor, and R. Sharman, 2018: Vertically propagating mountain waves—A hazard for high-flying aircraft? *J. Appl. Meteor. Climatol.*, **57**, 1957–1975, https://doi.org/10.1175/JAMC-D-17-0340.1.

Bushell, A. C., N. Butchart, S. H. Derbyshire, D. R. Jackson, G. J. Shutts, S. B. Vosper, and S. Webster, 2015: Parameterized gravity wave momentum fluxes from sources related to convection and large-scale precipitation processes in a global atmosphere model. *J. Atmos. Sci.*, **72**, 4349–4371, https://doi.org/10.1175/JAS-D-15-0022.1.

Butchart, N., 2014: The Brewer–Dobson circulation. *Rev. Geophys.*, **52**, 157–184, https://doi.org/10.1002/2013RG000448.

Callies, J., R. Ferrari, and O. Bühler, 2014: Transition from geostrophic turbulence to inertia–gravity waves in the atmospheric energy spectrum. *Proc. Natl. Acad. Sci. USA*, **111**, 17 033–17 038, https://doi.org/10.1073/pnas.1410772111.

——, O. Bühler, and R. Ferrari, 2016: The dynamics of mesoscale winds in the upper troposphere and lower stratosphere. *J. Atmos. Sci.*, **73**, 4853–4872, https://doi.org/10.1175/JAS-D-16-0108.1.

Chun, H., B. Song, S. Shin, and Y. Kim, 2019: Gravity waves associated with jet/front systems. Part I: Diagnostics and their correlations with GWs revealed in high-resolution global analysis data. *Asia-Pac. J. Atmos. Sci.*, **55**, 589–608, https://doi.org/10.1007/s13143-019-00104-1.

de la Cámara, A., F. Lott, and A. Hertzog, 2014: Intermittency in a stochastic parameterization of nonorographic gravity waves. *J. Geophys. Res. Atmos.*, **119**, 11 905–11 919, https://doi.org/10.1002/2014JD022002.

Dörnbrack, A., 2021: Stratospheric mountain waves trailing across northern Europe. *J. Atmos. Sci.*, **78**, 2835–2857, https://doi.org/10.1175/JAS-D-20-0312.1.

——, and Coauthors, 2018: Gravity waves excited during a minor sudden stratospheric warming. *Atmos. Chem. Phys.*, **18**, 12 915–12 931, https://doi.org/10.5194/acp-18-12915-2018.

Du, Y., F. Zhang, Y. Q. Sun, J. Wei, and X. Li, 2021: Practical and intrinsic predictability of wave-convection coupled bands over southern China. *J. Geophys. Res. Atmos.*, **126**, e2021JD034882, https://doi.org/10.1029/2021JD034882.

Dunkerton, T. J., and N. Butchart, 1984: Propagation and selective transmission of internal gravity waves in a sudden warming. *J. Atmos. Sci.*, **41**, 1443–1460, https://doi.org/10.1175/1520-0469(1984)041<1443:PASTOI>2.0.CO;2.

Ehard, B., S. Malardel, A. Dörnbrack, B. Kaifler, N. Kaifler, and N. Wedi, 2018: Comparing ECMWF high-resolution analyses with lidar temperature measurements in the middle atmosphere. *Quart. J. Roy. Meteor. Soc.*, **144**, 633–640, https://doi.org/10.1002/qj.3206.

Fritts, D. C., and M. J. Alexander, 2003: Gravity wave dynamics and effects in the middle atmosphere. *Rev. Geophys.*, **41**, 1003, https://doi.org/10.1029/2001RG000106.

——, and Coauthors, 2016: The Deep Propagating Gravity Wave Experiment (DEEPWAVE): An airborne and ground-based exploration of gravity wave propagation and effects from their sources throughout the lower and middle atmosphere. *Bull. Amer. Meteor. Soc.*, **97**, 425–453, https://doi.org/10.1175/BAMS-D-14-00269.1.

Geller, M. A., and Coauthors, 2013: A comparison between gravity wave momentum fluxes in observations and climate

models. *J. Climate*, **26**, 6383–6405, https://doi.org/10.1175/JCLI-D-12-00545.1.

Gong, J., D. L. Wu, and S. D. Eckermann, 2012: Gravity wave variances and propagation derived from AIRS radiances. *Atmos. Chem. Phys.*, **12**, 1701–1720, https://doi.org/10.5194/acp-12-1701-2012.

Greybush, S. J., E. Kalnay, T. Miyoshi, K. Ide, and B. R. Hunt, 2011: Balance and ensemble Kalman filter localization techniques. *Mon. Wea. Rev.*, **139**, 511–522, https://doi.org/10.1175/2010MWR3328.1.

Gupta, A., T. Birner, A. Dörnbrack, and I. Polichtchouk, 2021: Importance of gravity wave forcing for springtime southern polar vortex breakdown as revealed by ERA5. *Geophys. Res. Lett.*, **48**, e2021GL092762, https://doi.org/10.1029/2021GL092762.

Haynes, P., 2005: Stratospheric dynamics. *Annu. Rev. Fluid Mech.*, **37**, 263–293, https://doi.org/10.1146/annurev.fluid.37.061903.175710.

Hendricks, E., J. Doyle, S. Eckermann, Q. Jiang, and P. Reinecke, 2014: What is the source of the stratospheric gravity wave belt in austral winter? *J. Atmos. Sci.*, **71**, 1583–1592, https://doi.org/10.1175/JAS-D-13-0332.1.

Hersbach, H., and Coauthors, 2020: The ERA5 global reanalysis. *Quart. J. Roy. Meteor. Soc.*, **146**, 1999–2049, https://doi.org/10.1002/qj.3803.

Hien, S., J. Rolland, S. Borchert, L. Schoon, C. Zülicke, and U. Achatz, 2018: Spontaneous inertia–gravity wave emission in the differentially heated rotating annulus experiment. *J. Fluid Mech.*, **838**, 5–41, https://doi.org/10.1017/jfm.2017.883.

Hindley, N. P., C. J. Wright, L. Hoffmann, T. Moffat-Griffin, and N. J. Mitchell, 2020: An 18-year climatology of directional stratospheric gravity wave momentum flux from 3-D satellite observations. *Geophys. Res. Lett.*, **47**, e2020GL089557, https://doi.org/10.1029/2020GL089557.

Hoffmann, L., R. Spang, A. Orr, M. J. Alexander, L. A. Holt, and O. Stein, 2017: A decadal satellite record of gravity wave activity in the lower stratosphere to study polar stratospheric cloud formation. *Atmos. Chem. Phys.*, **17**, 2901–2920, https://doi.org/10.5194/acp-17-2901-2017.

Holt, L. A., M. J. Alexander, L. Coy, C. Liu, A. Molod, W. Putmanb, and S. Pawsonb, 2017: An evaluation of gravity waves and gravity wave sources in the Southern Hemisphere in a 7 km global climate simulation. *Quart. J. Roy. Meteor. Soc.*, **143**, 2481–2495, https://doi.org/10.1002/qj.3101.

Holton, J. R., and R. S. Lindzen, 1972: An updated theory for the quasi-biennial cycle of the tropical stratosphere. *J. Atmos. Sci.*, **29**, 1076–1080, https://doi.org/10.1175/1520-0469(1972)029<1076:AUTFTQ>2.0.CO;2.

——, P. H. Haynes, M. E. McIntyre, A. R. Douglass, R. B. Road, and L. Pfister, 1995: Stratosphere–troposphere exchange. *Rev. Geophys.*, **33**, 403–439, https://doi.org/10.1029/95RG02097.

Houghton, J. T., 1978: The stratosphere and mesosphere. *Quart. J. Roy. Meteor. Soc.*, **104**, 1–29, https://doi.org/10.1002/qj.49710443902.

Jewtoukoff, V., A. Hertzog, R. Plougonven, A. D. L. Cámara, and F. Lott, 2015: Comparison of gravity waves in the Southern Hemisphere derived from balloon observations and the ECMWF analyses. *J. Atmos. Sci.*, **72**, 3449–3468, https://doi.org/10.1175/JAS-D-14-0324.1.

Kaifler, N., B. Kaifler, A. Dörnbrack, M. Rapp, J. L. Hormaechea, and A. de la Torre, 2020: Lidar observations of large-amplitude mountain waves in the stratosphere above Tierra del Fuego, Argentina. *Sci. Rep.*, **10**, 14529, https://doi.org/10.1038/s41598-020-71443-7.

Kim, S.-Y., and H.-Y. Chun, 2010: Momentum flux of stratospheric gravity waves generated by Typhoon Ewiniar (2006). *Asia-Pac. J. Atmos. Sci.*, **46**, 199–208, https://doi.org/10.1007/s13143-010-0018-z.

Kim, Y.-J., S. D. Eckermann, and H. Y. Chun, 2003: An overview of the past, present and future of gravity-wave drag parametrization for numerical climate and weather prediction models. *Atmos.–Ocean*, **41**, 65–98, https://doi.org/10.3137/ao.410105.

Kim, Y.-H., H.-Y. Chun, P. Preusse, M. Ern, and S.-Y. Kim, 2012: Gravity wave reflection and its influence on the consistency of temperature- and wind-based momentum fluxes above Typhoon Ewiniar. *Atmos. Chem. Phys.*, **12**, 10 787–10 795, https://doi.org/10.5194/acp-12-10787-2012.

Koch, S. E., and Coauthors, 2005: Turbulence and gravity waves within an upper-level front. *J. Atmos. Sci.*, **62**, 3885–3908, https://doi.org/10.1175/JAS3574.1.

Koshyk, J. N., and K. Hamilton, 2001: The horizontal kinetic energy spectrum and spectral budget simulated by a high-resolution troposphere–stratosphere–mesosphere GCM. *J. Atmos. Sci.*, **58**, 329–348, https://doi.org/10.1175/1520-0469(2001)058<0329:THKESA>2.0.CO;2.

Kruse, C. G., and R. B. Smith, 2015: Gravity wave diagnostics and characteristics in mesoscale fields. *J. Atmos. Sci.*, **72**, 4372–4392, https://doi.org/10.1175/JAS-D-15-0079.1.

——, and Coauthors, 2022: Observed and modeled mountain waves from the surface to the mesosphere near the Drake Passage. *J. Atmos. Sci.*, **79**, 909–932, https://doi.org/10.1175/JAS-D-21-0252.1.

Lane, T. P., and F. Zhang, 2011: Coupling between gravity waves and tropical convection at mesoscales. *J. Atmos. Sci.*, **68**, 2582–2598, https://doi.org/10.1175/2011JAS3577.1.

——, J. D. Doyle, R. Plougonven, M. A. Shapiro, and R. D. Sharman, 2004: Observations and numerical simulations of inertia–gravity waves and shearing instabilities in the vicinity of a jet stream. *J. Atmos. Sci.*, **61**, 2692–2706, https://doi.org/10.1175/JAS3305.1.

Lehmann, C. I., Y.-H. Kim, P. Preusse, H.-Y. Chun, M. Ern, and S.-Y. Kim, 2012: Consistency between Fourier transform and small-volume few-wave decomposition for spectral and spatial variability of gravity waves above a typhoon. *Atmos. Meas. Tech.*, **5**, 1637–1651, https://doi.org/10.5194/amt-5-1637-2012.

Limpasuvan, V., J. H. Richter, Y. J. Orsolini, F. Stordal, and O. K. Kvissel, 2012: The roles of planetary and gravity waves during a major stratospheric sudden warming as characterized in WACCM. *J. Atmos. Sol.-Terr. Phys.*, **78–79**, 84–98, https://doi.org/10.1016/j.jastp.2011.03.004.

Lindzen, R. S., 1981: Turbulence and stress owing to gravity wave and tidal breakdown. *J. Geophys. Res.*, **86**, 9707–9714, https://doi.org/10.1029/JC086iC10p09707.

——, and K.-K. Tung, 1976: Banded convective activity and ducted gravity waves. *Mon. Wea. Rev.*, **104**, 1602–1617, https://doi.org/10.1175/1520-0493(1976)104<1602:BCAADG>2.0.CO;2.

Liu, H.-L., J. M. McInerney, S. Santos, P. H. Lauritzen, M. A. Taylor, and N. M. Pedatella, 2014: Gravity waves simulated by high-resolution Whole Atmosphere Community Climate Model. *Geophys. Res. Lett.*, **41**, 9106–9112, https://doi.org/10.1002/2014GL062468.

Lott, F., and M. J. Miller, 1997: A new subgrid-scale orographic drag parametrization: Its formulation and testing. *Quart. J. Roy. Meteor. Soc.*, **123**, 101–127, https://doi.org/10.1002/qj.49712353704.

Lu, Y., T. Wu, W. Jie, A. Scaife, M. Andrews, and J. Richter, 2020: Variability of the stratospheric quasi-biennial oscillation and its wave forcing simulated in the Beijing climate center atmospheric general circulation model. *J. Atmos. Sci.*, **77**, 149–165, https://doi.org/10.1175/JAS-D-19-0123.1.

Malardel, S., N. Wedi, W. Deconinck, M. Diamantakis, C. Kuehnlein, G. Mozdzynski, M. Hamrud, and P. Smolarkiewicz, 2016: A new grid for the IFS. *ECMWF Newsletter*, No. 146, ECMWF, Reading, United Kingdom, 23–28.

Matthias, V., A. Dörnbrack, and G. Stober, 2016: The extraordinarily strong and cold polar vortex in the early northern winter 2015/2016. *Geophys. Res. Lett.*, **43**, 12 287–12 294, https://doi.org/10.1002/2016GL071676.

Minamihara, Y., K. Sato, and M. Tsutsumi, 2020: Intermittency of gravity waves in the Antarctic troposphere and lower stratosphere revealed by the PANSY radar observation. *J. Geophys. Res. Atmos.*, **125**, e2020JD032543, https://doi.org/10.1029/2020JD032543.

Mirzaei, M., A. R. Mohebalhojeh, C. Zülicke, and R. Plougonven, 2017: On the quantification of imbalance and inertia–gravity waves generated in numerical simulations of moist baroclinic waves using the WRF Model. *J. Atmos. Sci.*, **74**, 4241–4263, https://doi.org/10.1175/JAS-D-16-0366.1.

Neale, R. B., and Coauthors, 2010: Description of the NCAR Community Atmospheric Model (CAM 4.0). NCAR Tech. Note NCAR/TN-485+STR, NCAR, 224 pp., www.cesm.ucar.edu/models/ccsm4.0/cam/docs/description/cam4_desc.pdf.

Orr, A., P. Bechtold, J. Scinocca, M. Ern, and M. Janiskova, 2010: Improved middle atmosphere climate and forecasts in the ECMWF model through a nonorographic gravity wave drag parameterization. *J. Climate*, **23**, 5905–5926, https://doi.org/10.1175/2010JCLI3490.1.

Plougonven, R., and F. Zhang, 2014: Internal gravity waves from atmospheric jets and fronts. *Rev. Geophys.*, **52**, 33–76, https://doi.org/10.1002/2012RG000419.

——, H. Teitelbaum, and V. Zeitlin, 2003: Inertia gravity wave generation by the tropospheric midlatitude jet as given by the fronts and Atlantic storm-track experiment radio soundings. *J. Geophys. Res.*, **108**, 4686, https://doi.org/10.1029/2003JD003535.

——, A. Hertzog, and L. Guez, 2013: Gravity waves over Antarctica and the Southern Ocean: Consistent momentum fluxes in mesoscale simulations and stratospheric balloon observations. *Quart. J. Roy. Meteor. Soc.*, **139**, 101–118, https://doi.org/10.1002/qj.1965.

——, A. de la Cámara, A. Hertzog, and F. Lott, 2020: How does knowledge of atmospheric gravity waves guide their parameterizations? *Quart. J. Roy. Meteor. Soc.*, **146**, 1529–1543, https://doi.org/10.1002/qj.3732.

Polichtchouk, I., and Coauthors, 2021: Stratospheric modelling and assimilation. ECMWF Tech. Memo. 877, ECMWF, 63 pp., https://doi.org/10.21957/25hegfoq.

——, N. Wedi, and Y.-H. Kim, 2022: Resolved gravity waves in the tropical stratosphere: Impact of horizontal resolution and deep convection parametrization. *Quart. J. Roy. Meteor. Soc.*, **148**, 233–251, https://doi.org/10.1002/qj.4202.

Powers, J. G., 1997: Numerical model simulation of a mesoscale gravity wave event: Sensitivity tests and spectral analysis. *Mon. Wea. Rev.*, **125**, 1838–1869, https://doi.org/10.1175/1520-0493(1997)125<1838:NMSOAM>2.0.CO;2.

Preusse, P., M. Ern, P. Bechtold, S. D. Eckermann, S. Kalisch, Q. T. Trinh, and M. Riese, 2014: Characteristics of gravity waves resolved by ECMWF. *Atmos. Chem. Phys.*, **14**, 10 483–10 508, https://doi.org/10.5194/acp-14-10483-2014.

Qian, T., F. Zhang, J. Wei, J. He, and Y. Lu, 2020: Diurnal characteristics of gravity waves over the Tibetan Plateau in 2015 summer using 10-km downscaled simulations from WRF-EnKF regional reanalysis. *Atmosphere*, **11**, 631, https://doi.org/10.3390/atmos11060631.

Ribstein, B., U. Achatz, and F. Senf, 2015: The interaction between gravity waves and solar tides: Results from 4-D ray tracing coupled to a linear tidal model. *J. Geophys. Res. Space Phys.*, **120**, 6795–6817, https://doi.org/10.1002/2015JA021349.

Richter, J. H., F. Sassi, and R. R. Garcia, 2010: Toward a physically based gravity wave source parameterization in a general circulation model. *J. Atmos. Sci.*, **67**, 136–156, https://doi.org/10.1175/2009JAS3112.1.

Ruppert, J. H., S. E. Koch, X. Chen, Y. Du, A. Seimon, Y. Q. Sun, J. Wei, and L. F. Bosart, 2022: Mesoscale gravity waves and midlatitude weather: A tribute to Fuqing Zhang. *Bull. Amer. Meteor. Soc.*, **103**, E129–E156, https://doi.org/10.1175/BAMS-D-20-0005.1.

Sato, K., S. Watanabe, Y. Kawatani, Y. Tomikawa, K. Miyazaki, and M. Takahashi, 2009: On the origins of mesospheric gravity waves. *Geophys. Res. Lett.*, **36**, L19801, https://doi.org/10.1029/2009GL039908.

——, R. Yasui, and Y. Miyoshi, 2018: The momentum budget in the stratosphere, mesosphere, and lower thermosphere. Part I: Contributions of different wave types and in situ generation of Rossby waves. *J. Atmos. Sci.*, **75**, 3613–3633, https://doi.org/10.1175/JAS-D-17-0336.1.

Scinocca, J. F., 2003: An accurate spectral nonorographic gravity wave drag parameterization for general circulation models. *J. Atmos. Sci.*, **60**, 667–682, https://doi.org/10.1175/1520-0469(2003)060<0667:AASNGW>2.0.CO;2.

Shapiro, M. A., 1980: Turbulent mixing within tropopause folds as a mechanism for the exchange of chemical constituents between the stratosphere and troposphere. *J. Atmos. Sci.*, **37**, 994–1004, https://doi.org/10.1175/1520-0469(1980)037<0994:TMWTFA>2.0.CO;2.

Shutts, G. J., and S. B. Vosper, 2011: Stratospheric gravity waves revealed in NWP model forecasts. *Quart. J. Roy. Meteor. Soc.*, **137**, 303–317, https://doi.org/10.1002/qj.763.

Stephan, C. C., C. Strube, D. Klocke, M. Ern, L. Hoffmann, P. Preusse, and H. Schmidt, 2019a: Intercomparison of gravity waves in global convection-permitting models. *J. Atmos. Sci.*, **76**, 2739–2759, https://doi.org/10.1175/JAS-D-19-0040.1.

——, ——, ——, ——, ——, ——, and ——, 2019b: Gravity waves in global high-resolution simulations with explicit and parameterized convection. *J. Geophys. Res. Atmos.*, **124**, 4446–4459, https://doi.org/10.1029/2018JD030073.

——, T. P. Lane, and C. Jakob, 2020: Gravity wave influences on mesoscale divergence: An observational case study. *Geophys. Res. Lett.*, **47**, e2019GL086539, https://doi.org/10.1029/2019GL086539.

Strube, C., P. Preusse, M. Ern, and M. Riese, 2021: Propagation paths and source distributions of resolved gravity waves in ECMWF-IFS analysis fields around the southern polar night jet. *Atmos. Chem. Phys.*, **21**, 18 641–18 668, https://doi.org/10.5194/acp-21-18641-2021.

Sun, Y. Q., and F. Zhang, 2016: Intrinsic versus practical limits of atmospheric predictability and the significance of the butterfly effect. *J. Atmos. Sci.*, **73**, 1419–1438, https://doi.org/10.1175/JAS-D-15-0142.1.

——, R. Rotunno, and F. Zhang, 2017: Contributions of moist convection and internal gravity waves to building the atmospheric −5/3 kinetic energy spectra. *J. Atmos. Sci.*, **74**, 185–201, https://doi.org/10.1175/JAS-D-16-0097.1.

Uccellini, L. W., and S. E. Koch, 1987: The synoptic setting and possible energy sources for mesoscale wave disturbances. *Mon. Wea. Rev.*, **115**, 721–729, https://doi.org/10.1175/1520-0493(1987)115<0721:TSSAPE>2.0.CO;2.

Wang, L., and M. A. Geller, 2003: Morphology of gravity-wave energy as observed from 4 years (1998–2001) of high vertical resolution U.S. radiosonde data. *J. Geophys. Res.*, **108**, 4489, https://doi.org/10.1029/2002JD002786.

Wang, S., F. Zhang, and C. Snyder, 2009: Generation and propagation of inertia-gravity waves from vortex dipoles and jets. *J. Atmos. Sci.*, **66**, 1294–1314, https://doi.org/10.1175/2008JAS2830.1.

Warner, C. D., and M. E. McIntyre, 2001: An ultrasimple spectral parameterization for nonorographic gravity waves. *J. Atmos. Sci.*, **58**, 1837–1857, https://doi.org/10.1175/1520-0469(2001)058<1837:AUSPFN>2.0.CO;2.

Watanabe, S., Y. Kawatani, Y. Tomikawa, K. Miyazaki, M. Takahashi, and K. Sato, 2008: General aspects of a T213L256 middle atmosphere general circulation model. *J. Geophys. Res.*, **113**, D12110, https://doi.org/10.1029/2008JD010026.

Wedi, N. P., 2014: Increasing horizontal resolution in numerical weather prediction and climate simulations: Illusion or panacea? *Philos. Trans. Roy. Soc.*, **372A**, 20130289, https://doi.org/10.1098/rsta.2013.0289.

——, and Coauthors, 2020: A baseline for global weather and climate simulations at 1 km resolution. *J. Adv. Model. Earth Syst.*, **12**, e2020MS002192, https://doi.org/10.1029/2020MS002192.

Wei, J., and F. Zhang, 2014: Mesoscale gravity waves in moist baroclinic jet–front systems. *J. Atmos. Sci.*, **71**, 929–952, https://doi.org/10.1175/JAS-D-13-0171.1.

——, and ——, 2015: Tracking gravity waves in moist baroclinic jet-front systems. *J. Adv. Model. Earth Syst.*, **7**, 67–91, https://doi.org/10.1002/2014MS000395.

——, ——, and J. H. Richter, 2016: An analysis of gravity wave spectral characteristics in moist baroclinic jet–front systems. *J. Atmos. Sci.*, **73**, 3133–3155, https://doi.org/10.1175/JAS-D-15-0316.1.

——, G. Bölöni, and U. Achatz, 2019: Efficient modeling of the interaction of mesoscale gravity waves with unbalanced large-scale flows: Pseudomomentum-flux convergence versus direct approach. *J. Atmos. Sci.*, **76**, 2715–2738, https://doi.org/10.1175/JAS-D-18-0337.1.

Wilhelm, J., T. Akylas, G. Bölöni, J. Wei, B. Ribstein, R. Klein, and U. Achatz, 2018: Interactions between mesoscale and submesoscale gravity waves and their efficient representation in mesoscale-resolving models. *J. Atmos. Sci.*, **75**, 2257–2280, https://doi.org/10.1175/JAS-D-17-0289.1.

Yamashita, C., H.-L. Liu, and X. Chu, 2010: Gravity wave variations during the 2009 stratospheric sudden warming as revealed by ECMWF-T799 and observations. *Geophys. Res. Lett.*, **37**, L22806, https://doi.org/10.1029/2010GL045437.

Žagar, N., A. Kasahara, K. Terasaki, J. Tribbia, and H. Tanaka, 2015a: Normal-mode function representation of global 3-D data sets: Open-access software for the atmospheric research community. *Geosci. Model Dev.*, **8**, 1169–1195, https://doi.org/10.5194/gmd-8-1169-2015.

——, R. Buizza, and J. Tribbia, 2015b: A three-dimensional multivariate modal analysis of atmospheric predictability with application to the ECMWF ensemble. *J. Atmos. Sci.*, **72**, 4423–4444, https://doi.org/10.1175/JAS-D-15-0061.1.

——, D. Jelić, M. Blaauw, and P. Bechtold, 2017: Energy spectra and inertia–gravity waves in global analyses. *J. Atmos. Sci.*, **74**, 2447–2466, https://doi.org/10.1175/JAS-D-16-0341.1.

Zhang, F., 2004: Generation of mesoscale gravity waves in the upper-tropospheric jet–front systems. *J. Atmos. Sci.*, **61**, 440–457, https://doi.org/10.1175/1520-0469(2004)061<0440:GOMGWI>2.0.CO;2.

——, S. E. Koch, C. A. Davis, and M. L. Kaplan, 2001: Wavelet analysis and the governing dynamics of a large-amplitude mesoscale gravity-wave event along the east coast of the United States. *Quart. J. Roy. Meteor. Soc.*, **127**, 2209–2245, https://doi.org/10.1002/qj.49712757702.

——, N. Bei, R. Rotunno, C. Snyder, and C. C. Epifanio, 2007: Mesoscale predictability of moist baroclinic waves: Convection-permitting experiments and multistage error growth dynamics. *J. Atmos. Sci.*, **64**, 3579–3594, https://doi.org/10.1175/JAS4028.1.

——, M. Zhang, J. Wei, and S. Wang, 2013: Month-long simulations of gravity waves over North America and North Atlantic in comparison with satellite observations. *Acta Meteor. Sin.*, **27**, 446–454, https://doi.org/10.1007/s13351-013-0301-x.

——, J. Wei, M. Zhang, K. P. Bowman, L. L. Pan, E. Atlas, and S. C. Wofsy, 2015: Aircraft measurements of gravity waves in the upper troposphere and lower stratosphere during the START08 field experiment. *Atmos. Chem. Phys.*, **15**, 7667–7684, https://doi.org/10.5194/acp-15-7667-2015.

——, Y. Q. Sun, L. Magnusson, R. Buizza, S.-J. Lin, J.-H. Chen, and K. Emanuel, 2019: What is the predictability limit of midlatitude weather? *J. Atmos. Sci.*, **76**, 1077–1091, https://doi.org/10.1175/JAS-D-18-0269.1.